Computer Methods in Applied Mechanics and Engineering 420 (2024) 116724

Contents lists available at ScienceDirect

Comput. Methods Appl. Mech. Engrg.

journal homepage: www.elsevier.com/locate/cma

Whole-heart modelling with valves in a fluid–structure interaction framework

Liuyang Feng *, Hao Gao, Xiaoyu Luo

School of Mathematics and Statistics, University of Glasgow, Glasgow, G12 8QQ, UK

ARTICLE INFO

Keywords:
Whole-heart modelling
Heart valves
Fluid–structure interaction

ABSTRACT

Computational modelling of whole-heart function is a useful tool to study heart mechanics and haemodynamics. Many existing heart models focus on electromechanical aspect without considering physiological valves and use simplified fluid models instead. In this study we develop a four-chamber heart model featuring realistic chamber geometry, detailed valve modelling, hyperelasticity with fibre architecture and fluid–structure interaction analysis. Our model is used to investigate heart behaviours with different modelling assumptions including restricted/free valve annular dynamics, and with/without heart-pericardium interactions. Our simulation results capture the interactions between valve leaflet and surrounding flow, typical left ventricular flow vortices, typical venous and transvalvular flow waveform, and physiological heart deformations such as atrioventricular plane movement. The improvement of ventricular filling and atrial emptying at early diastole is evident with free annulus. In addition, we find that the added pericardial forces on the heart have a predominant effect on atrial wall deformation especially during atrial contraction, and further help with the atrial filling process. Most importantly, the current study provides a framework for comprehensive multi-physics whole-heart modelling considering all heart valves and fluid–structure interactions.

1. Introduction

The heart is arguably the most important organ inside the human body. On average, a heart beats more than 2.8 billion times during its lifetime and every single heartbeat requires the cooperation of different biological processes across different scales in time and space [1] such as electrical potential propagation and biochemical reactions at the cellular level, myofilament tension development and relaxation at cellular and tissue level, electromechanics at the tissue level and haemodynamics at the organ level, etc. To better understand the complex heart function, numerous research effort has been devoted over the years among which computational modelling [2–5] has gained popularity due to the development of cardiac imaging technology [6] and computational power [7].

Existing computational heart models can be divided into local [2,8–16] and global models [4,17–19] according to the completeness of heart geometry, or single physics and multi-physics with focuses on different biological processes such as electrophysiology [20], tissue mechanics [21,22] and haemodynamics [23]. Among the existing whole-heart models, valve modelling is often simplified. As a result, heart haemodynamics is usually represented via lumped-parameter models [18,24] within closed chambers, or simulated either with zero-volumetric valve model such as resistive immersed surface (RIS) approach [17,25] or

* Corresponding author.
E-mail address: Liuyang.Feng@glasgow.ac.uk (L. Feng).

https://doi.org/10.1016/j.cma.2023.116724
Received 31 August 2023; Received in revised form 24 December 2023; Accepted 24 December 2023

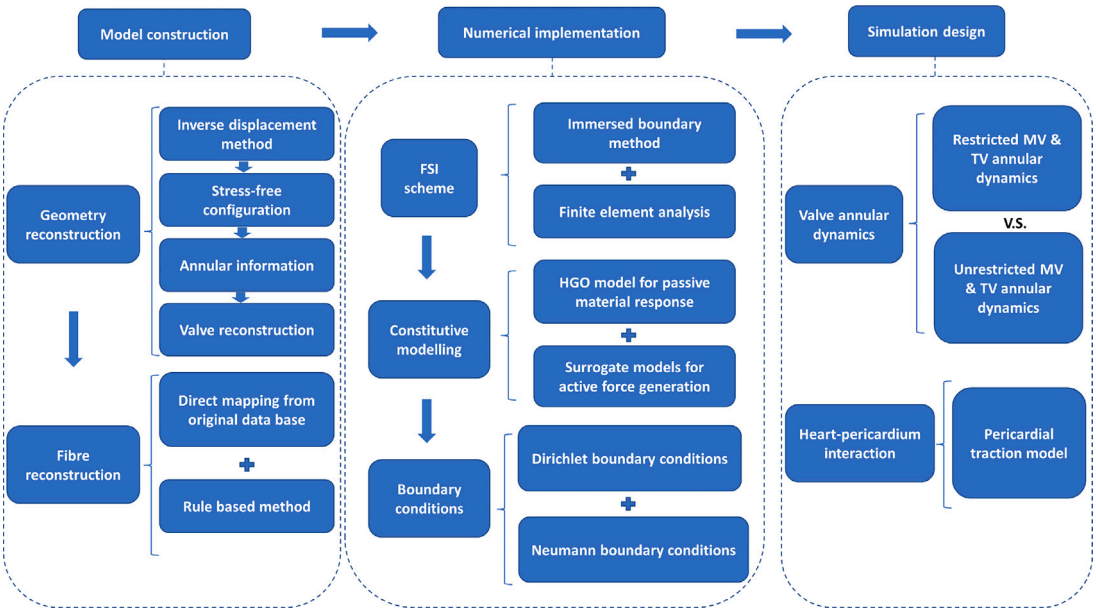

Fig. 1. A schematic diagram for the model development process.

with prescribed heart wall and valve motions [15,16]. Such approaches do reduce model complexity. However, as one of the most important components in coordinating heart flow [26,27], fully three-dimensional valve modelling with fluid–structure interaction (FSI) must be considered to capture realistic heart haemodynamics in fine-scales [28,29]. Additionally, incorporation of valve modelling into whole-heart models brings benefits of improved understanding of pathological conditions with the connection between haemodynamic alterations [30] and heart structural changes (cardiac growth and remodelling). For example, in the case of pulmonary hypertension caused by left heart disease [31], only whole-heart models with valves and fluid–structure interaction included can thoroughly investigate the disease progression from the original left heart valve dysfunction (common cause) to the pressure elevation inside the pulmonary circulation, and finally to the right heart failure. The challenges of valve modelling come from complicated valve leaflet/chordae geometry and large deformation caused by leaflet-blood interactions that can significantly increase the overall heart model complexity.

To the best of the authors' knowledge, only a handful of whole-heart models have incorporated full fluid–structure interaction with physiologically detailed four-chamber geometry and representation of all four heart valves [32,33]. Davey et al. [32] aimed to establish a comprehensive benchmark model for cardiac fluid dynamics, while Zingaro et al. [33] simplified valve structures through resistive immersed implicit surface methods. In the present work, we introduce a whole-heart FSI model utilizing an immersed boundary framework, encompassing patient-specific four-chamber geometry, anatomically precise valve representations, hyperelasticity featuring fibre architecture, and the incorporation of pericardium-heart interactions. Notably, the active contraction of heart chambers is modelled using surrogate models [22,34], while detailed electrophysiology is not included. Our primary objective is to provide comprehensive insights into the intricate mechanical dynamics and haemodynamics of the whole heart under physiological conditions. Of particular significance, this study marks the first investigation into the impact of valve annular dynamics and pericardium-heart interactions on overall heart function within a whole-heart FSI framework, supplemented by detailed energy budget analysis.

The subsequent sections of this paper are organized as follows: Section 2 presents the specifics of the whole-heart model, the immersed boundary framework, and the simulation design. Numerical results are outlined in Section 3, followed by in-depth discussions in Section 4. The paper concludes with a summary of findings in Section 5.

2. Modelling approach

The overall whole-heart model development can be divided into three main stages as shown in Fig. 1. Specifically,

- model construction which consists of heart geometry reconstruction and myocardial fibre reconstruction;
- numerical implementation which includes the numerical implementation of the FSI scheme and boundary conditions, and the characterization of material properties;
- simulation design for choosing the appropriate boundary conditions.

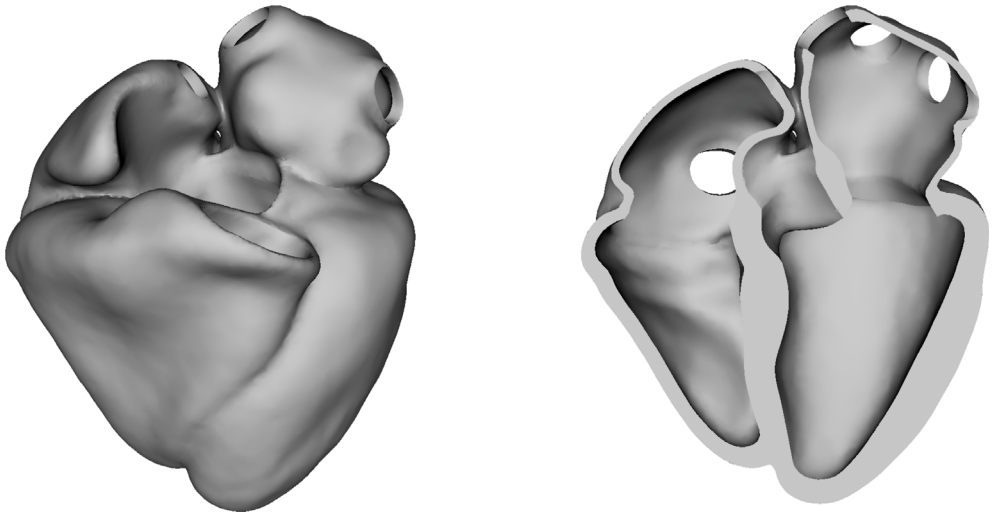

Fig. 2. The final four-chamber geometry in the stress-free state.

2.1. Building heart geometry

2.1.1. Four-chamber geometry

The heart geometry is obtained from a public virtual cohort of four-chamber heart meshes, which are built from 24 heart failure patients by Strocchi et al. [35]. In summary, they use end-diastolic computerised tomography (CT) scans for the image segmentation process with an automatic segmentation algorithm. The final four-chamber geometry includes the left/right ventricle (LV and RV), left/right atrium (LA and RA), aortic root, part of the ascending aorta and main pulmonary artery. Pulmonary veins and superior/inferior vena cava are not included while their connection sites to atria can be identified. Additionally, all heart valves, chordae tendinae and left atrium appendage are not included, and artificial orifice planes are constructed representing valve annulus location and vessel insertion sites.

A manual geometry selection process is conducted first to pick the most suitable four-chamber geometry for simulating normal heart physiology. Among these 24 hearts, geometric irregularities are often present such as significant chamber size differences between left and right ventricles, pulmonary vein anatomy variations (conjoined veins), etc. Since this work aims to develop a general framework for whole-heart modelling rather than a patient-specific heart model, a "normal" heart in terms of morphology is prioritized in the selection process. As a result, we select heart No. 18 based on its regularities of vessel number (i.e. four pulmonary veins), vessel insertion location (i.e. no conjoined vessels) and vessel orifice size (Table 1), heart chamber size (LV: 194 mL, RV: 143 mL, LA: 57 mL, RA: 62 mL) and shape (i.e. no skewed geometry). Finally, minor geometry modifications are made manually such as the removal of artificial orifice planes and construction of auxiliary structures including artificial arteries and veins (Fig. 12).

Another important step before introducing heart valves is to obtain a stress-free (unloaded) configuration for the four-chamber geometry, which is required for forward simulations without pre-stress. The original heart geometry was reconstructed using end-diastolic CT images [35] when both ventricles are fully loaded under end-diastolic pressure and both atria have completed active contraction. To simplify the process of obtaining a stress-free configuration for all chambers, we make the following assumptions: the original atrial geometry is stress-free at end diastole, and the end-diastolic cavity pressure is 8 mmHg in LV and 2 mmHg in RV, which are within the normal range [36,37]. Note the assumption of a stress-free state at the end of active contraction has been adopted in the literature [38].

Following the study by Wang et al. [39], we use an inverse displacement approach to obtain the unloaded ventricles. In short, the original end-diastolic geometry is taken as the initial guess of the unloaded configuration, and the assumed end-diastolic cavity pressures are applied to the ventricular endocardial surfaces to obtain a computed end-diastolic ventricle geometry while atria remain fixed. The difference in displacement between the computed and the original end-diastolic geometry is then used to update the guessed unloaded configuration. The whole procedure is repeated until the convergence is reached, and the cavity volume difference between the final computed end-diastolic ventricle geometry and the original ventricle geometry is 1.4% for LV and 2.7% for RV. Fig. 2 shows the final stress-free four-chamber geometry with details listed in Table 1.

2.1.2. Mitral valve (MV)

In order to capture more realistic transvalvular flow patterns and haemodynamics within heart chambers, all four valves (i.e. mitral and tricuspid valve, aortic and pulmonary valve) which are the key components of FSI analysis in whole heart modelling are included in the current model.

We use our previously developed mitral valve model [40] as shown in Fig. 3 (Left) in this study. The valve geometry is reconstructed by Wang and Sun [41] based on patient CT scans which contain valve annulus, leaflet and chordae tendinae

Table 1
Details of the stress-free four-chamber geometry. LSPV/LIPV: left superior and inferior pulmonary vein. RSPV/RIPV: right superior and inferior pulmonary vein. SVC/IVC: superior and inferior vena cava. Mean annulus diameter is calculated as the mean of the maximum and minimum annulus diameter.

	Cavity volume	Mean annulus diameter
LV	98 mL	–
RV	84 mL	–
LA	57 mL	–
RA	62 mL	–
MV	–	3.4 cm
TV	–	4.3 cm
AV	–	3.4 cm
PAV	–	3.2 cm
LSPV	–	1.4 cm
LIPV	–	1.5 cm
RSPV	–	1.5 cm
RIPV	–	1.5 cm
SVC	–	1.2 cm
IVC	–	1.7 cm

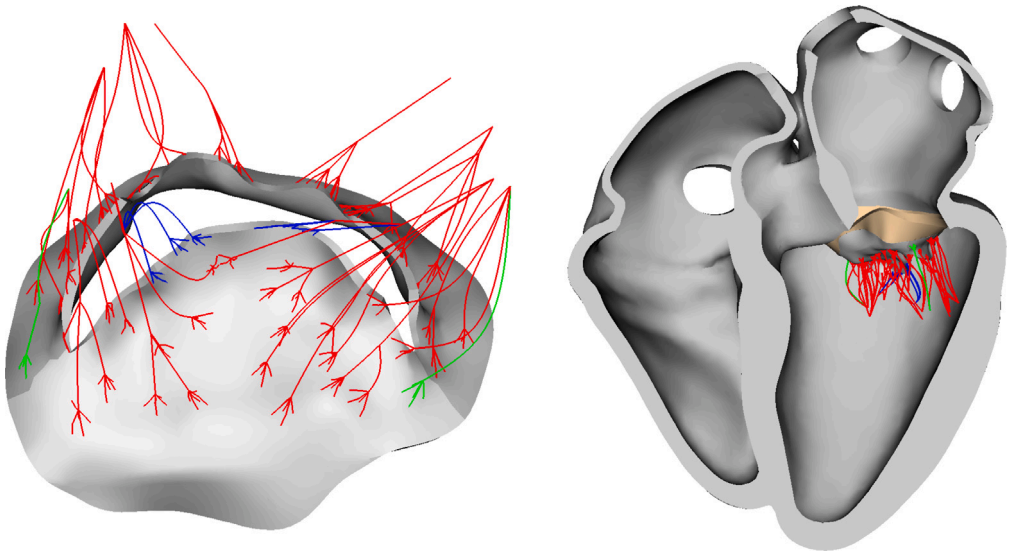

Fig. 3. (Left) Mitral valve geometry with chordae highlighted (strut chordae in red, basal chordae in green and marginal chordae in blue). (Right) Mitral valve mounted on the four-chamber geometry with housing highlighted. (For interpretation of the references to colour in this figure legend, the reader is referred to the web version of this article.)

information. Both anterior and posterior leaflets were assumed to have a uniform thickness of 2 mm with a total circumference of 125 mm for the valve annulus. In terms of chordae structure, 10 chordae originate from anterolateral papillary muscle and 11 from posterolateral papillary muscle, which is further classed as strut, basal and marginal chordae highlighted in Fig. 3(Left). To merge the valve geometry with the four-chamber geometry, we follow our previous approach [34] which involves annulus orientation matching, size matching and the construction of an auxiliary housing structure as shown in Fig. 3(Right). Papillary muscles are not included in the current model. However, to account for their functionalities, displacement boundary conditions are applied to the chordae origins [41].

2.1.3. Tricuspid valve (TV)

The tricuspid valve is constructed based on studies by Stevanella et al. [42] and Hiro et al. [43]. In the work by Stevanella et al. [42], valve geometric details such as annulus perimeter, leaflet and commissure height, and chordae tendinae number, etc., are reported from excised human and porcine tricuspid valves. In addition, Hiro et al. [43] manage to record three-dimensional annulus coordinates, valve leaflets opening angle and papillary muscle location using implanted ultrasonic crystals on adult sheep.

With the information from these two studies, the valve leaflet geometry construction starts with obtaining three-dimensional annulus information from the four-chamber geometry. Then, the free edges of the valve leaflets are constructed as B-splines using

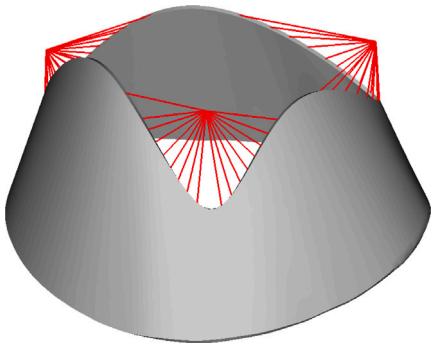

Fig. 4. Tricuspid valve geometry with chordae.

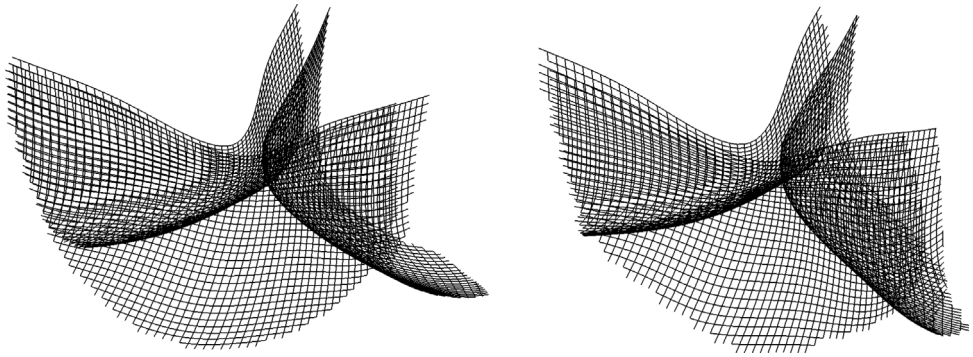

Fig. 5. Final (Left) aortic valve and (Right) pulmonary valve represented in pseudo fibres.

re-scaled data from Stevanella et al. [42] including the maximum height of each leaflet and the height of commissures, and also the leaflets opening angles from Hiro et al. [43]. In terms of chordae structure, we construct 17 chordae for the anterior and the posterior papillary muscle each, 19 chordae for the septal papillary muscle [43]. All chordaes are connected to the leaflets' free edge and evenly distributed. The chordae origins are decided using the reported data [43]. All leaflets are assumed to have a uniform thickness of 0.5 mm and the chordae cross-section area is assumed to be 0.16 mm^2. Fig. 4 shows the final tricuspid valve geometry with chordae structure.

2.1.4. Aortic valve (AV) and pulmonary valve (PAV)

The construction of the aortic valve starts with obtaining aortic root details from the original four-chamber geometry. To simplify the valve construction process, we only acquire the aortic sinus diameter from the heart geometry. Other aortic root dimensions such as the diameter of the ventriculo-arterial junction and the sinotubular junction, the height of the aortic sinuses, etc., are all computed using the reported data by Reul et al. [44] which results in an idealized aortic root geometry description. Next, following the approach presented by [45,46] and combing aortic root dimensions, an idealized aortic valve geometry is constructed. The final step is to place the aortic valve into the original aortic root and remove the excessive part for a water-tight connection.

Since the aortic valve and pulmonary valve share very similar geometric characteristics [47], we use the same procedure to construct an idealized pulmonary valve. Both valves are modelled by a system of pseudo fibres which resist extension, compression and bending [46] and the final valve models are presented in Fig. 5.

2.1.5. Fibre structure

Myocardial fibre structure plays an important role in heart mechanical response including both passive material anisotropy and active force generation. The anatomy of heart fibres has been thoroughly investigated in previous research [48–50]. In the area of computational modelling, personalized fibre structure reconstruction is possible via diffusion tensor magnetic resonance imaging (DTMRI) data [51]. However, the rule-based method remains the most popular one in heart modelling [52–54]. In this section, we give an overview of the reconstructed fibre structure for heart chambers and valves.

Ventricular fibre structures are well studied and commonly defined via rule-based methods with transmural changes in fibre orientations due to thick myocardium walls, especially in LV [55]. A secondary "sheet" structure perpendicular to the local fibre orientation is also needed for realistic wall deformation [56]. To reduce the workload, the current model borrows ventricular fibre and sheet structures from the original dataset [35] via direct mapping. The fibre and sheet orientations are defined using a rule-based method [52] in which the fibre orientation varies linearly from 80° (endocardium) to −60° (epicardium) and the sheet orientation

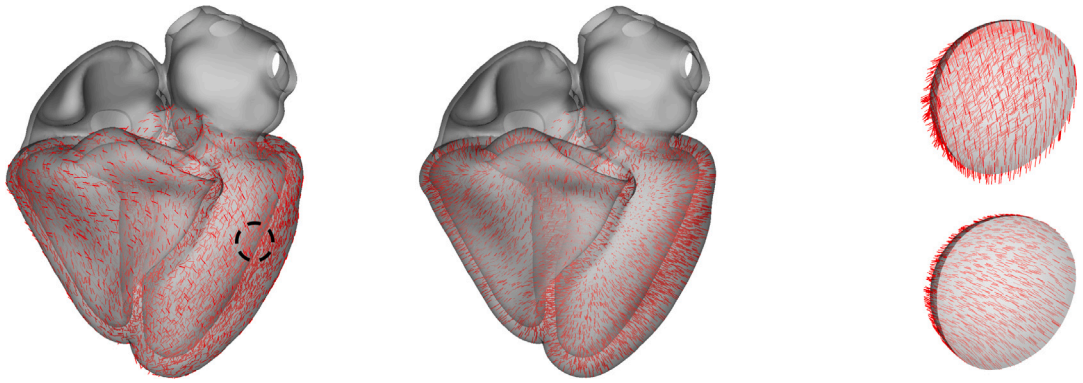

Fig. 6. (Left) Fibre orientation and (Mid) sheet orientation in ventricles. (Right) Zoom-in view of fibre and sheet orientations in the left ventricle (circled region).

varies linearly from −65° (endocardium) to 25° (epicardium). Fig. 6 shows an overview of the final fibre and sheet structure in ventricles.

In terms of atrial fibre reconstruction, atlas-based methods [57,58] and a recently proposed sophisticated Laplace–Dirichlet rule-based method are also available [54] in the literature. In this work, we follow our previous study [59] which uses a rule-based method with manually defined fibre regions on LA walls to account for experimentally observed muscle bundles such as Bachmann's bundle, septopulmonary bundle and septoatrial bundle [48]. Circumferentially oriented fibres are defined near the atrioventricular junction and vessel insertion sites. We have shown previously that such an approach leads to very similar LA mechanical behaviours to a complex atlas-based method [59]. Right atrium (RA) fibres are defined in a similar fashion. In detail, a total of nine regions as highlighted in Fig. 7 are defined on RA walls including circular regions near superior/inferior vena cava (SVC/IVC), intercaval region, crista terminalis region, lateral wall, anterior wall, septum, appendage and vestibule. Each region is assigned with a predominant fibre orientation to account for the observed fibre morphology [48]. For instance, circumferential directions are used for the circular regions, appendage and vestibule w.r.t their orifice. The anterior wall is defined with fibres parallel to the atrioventricular junction to represent the anterior interatrial band or Bachmann's bundle, and crista terminalis region has fibres following the superior-inferior axis. The lateral wall and intercaval region are defined with obliquely aligned fibres to account for the pectinate muscle and the intercaval bundle. The Septum region is defined with the same fibre orientations mapped from the LA septum. Unlike ventricles, transmural changes in fibre orientations and the secondary sheet structure are not considered for atria due to their thin walls. Fig. 7 shows the final fibre structure.

In the current study, the mitral valve is defined with two families of fibres [41], and circumferential fibres are defined for tricuspid valve leaflets [60] as demonstrated in Fig. 8. The material anisotropy for aortic and pulmonary valves is achieved with inhomogeneous spring stiffness and bending stiffness (Eqs. (17) and (18)) since they are modelled as a system of springs and beams.

2.2. Numerical methods

The fluid–structure interactions between the heart and blood flow are captured in an immersed boundary framework with finite element analysis [61,62]. The whole computational domain Ω is divided into solid region Ω^{s} and fluid region Ω^{f}. Let $\mathbf{X} \in \Omega^{\mathrm{s}}$ represent any material point on the solid in the reference configuration and $\chi(\mathbf{X}, t) \in \Omega$ defines an isomorphism mapping of each material point to its current physical position at any given time t. Therefore, the current deformed structure is denoted as $\Omega_t^{\mathrm{s}} = \chi(\Omega^{\mathrm{s}}, t)$ and $\Omega_t^{\mathrm{f}} = \Omega \backslash \Omega_t^{\mathrm{s}}$ is the current fluid region at time t.

The entire domain Ω is discretized via a Cartesian grid with coordinates $\mathbf{x} \in \Omega$ on which the momentum equation is solved via finite difference methods. The solid structure Ω_t^{s} interacts with the background grid via a delta function $\delta(\mathbf{x})$ which communicates force and velocity information between the Eulerian and Lagrangian coordinates. The governing equations are as follows

$$\rho\left(\frac{\partial \mathbf{u}(\mathbf{x},t)}{\partial t} + \mathbf{u}(\mathbf{x},t)\cdot\nabla\mathbf{u}(\mathbf{x},t)\right) = -\nabla p(\mathbf{x},t) + \mu\nabla^2\mathbf{u}(\mathbf{x},t) + \mathbf{f}(\mathbf{x},t), \tag{1}$$

$$\nabla\cdot\mathbf{u}(\mathbf{x},t) = 0, \tag{2}$$

$$\mathbf{f}(\mathbf{x},t) = \int_{\Omega^{\mathrm{s}}} \mathbf{F}(\mathbf{X},t)\ \delta(\mathbf{x} - \chi(\mathbf{X},t))\,\mathrm{d}\mathbf{X}, \tag{3}$$

$$\int_{\Omega^{\mathrm{s}}} \mathbf{F}(\mathbf{X},t)\cdot\mathbf{V}(\mathbf{X})\,\mathrm{d}\mathbf{X} = -\int_{\Omega^{\mathrm{s}}} \mathbb{P}^{\mathrm{e}}(\mathbf{X},t) : \nabla_{\mathbf{X}}\mathbf{V}(\mathbf{X})\mathrm{d}\mathbf{X} + \int_{\partial\Omega^{\mathrm{s}}} \mathbf{F}_{\mathrm{b}}(\mathbf{X},t)\cdot\mathbf{V}(\mathbf{X})\mathrm{d}A(\mathbf{X}),\ \forall\mathbf{V}(\mathbf{X}), \tag{4}$$

$$\frac{\partial\chi}{\partial t}(\mathbf{X},t) = \mathbf{u}(\chi(\mathbf{X},t),t) = \int_{\Omega}\mathbf{u}(\mathbf{x},t)\ \delta(\chi(\mathbf{X},t) - \mathbf{x})\,\mathrm{d}\mathbf{x}, \tag{5}$$

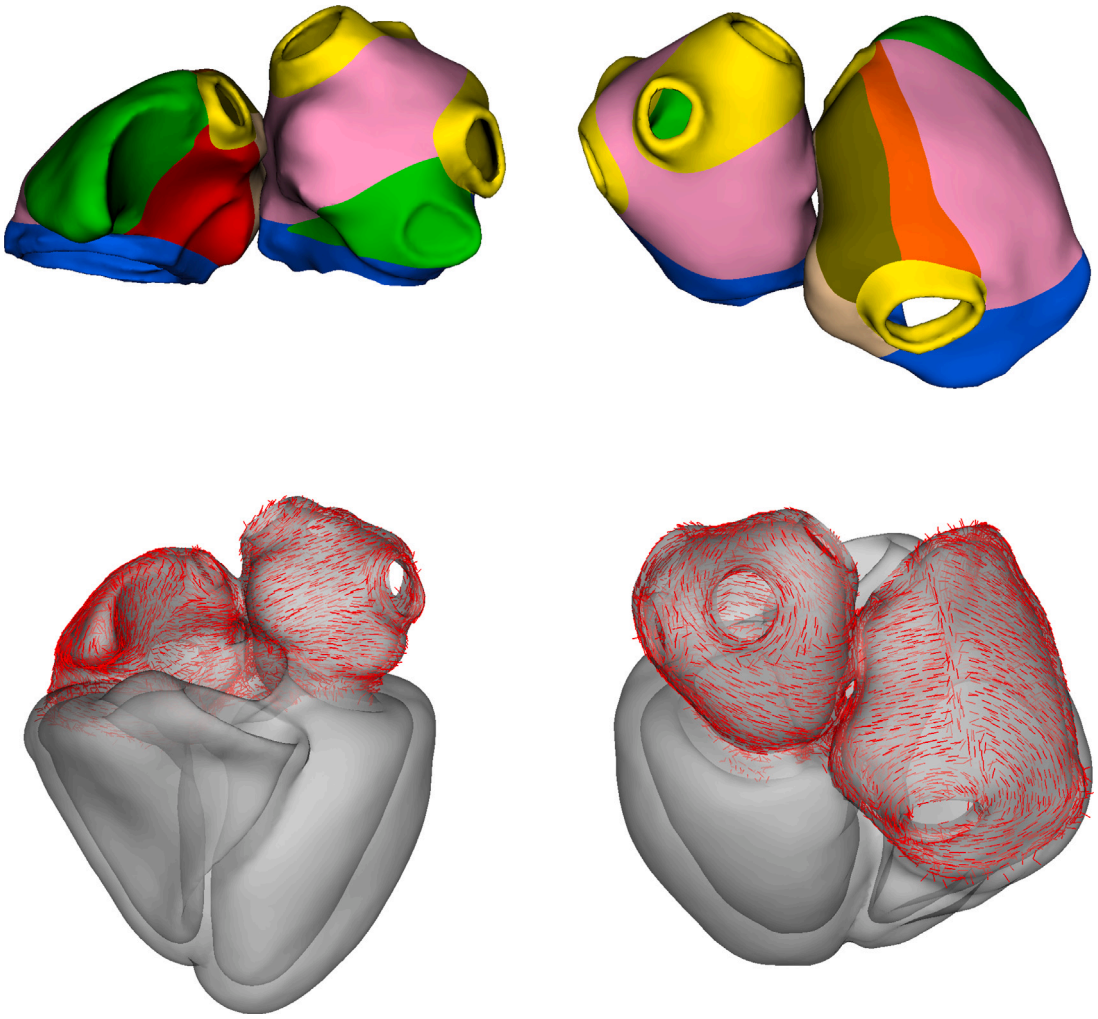

Fig. 7. Different regions (colored) defined for atrial fibre definition (Top row). Final atrial fibre orientation (Bottom row). (For interpretation of the references to colour in this figure legend, the reader is referred to the web version of this article.)

where Eqs. (1) and (2) are the momentum equation and the continuity equation with incompressibility constraint, and $\mathbf{u}(\mathbf{x},t)$, $p(\mathbf{x},t)$ denote the Eulerian velocity and pressure. ρ and μ are the constant material density and dynamic viscosity. Eqs. (3) and (5) demonstrate the interactions between Eulerian and Lagrangian coordinates via $\boldsymbol{\delta}(\mathbf{x})$, and Eq. (4) computes the Lagrangian force density $\mathbf{F}(\mathbf{X},t)$ for hyperelastic materials with $\mathbb{P}^{\mathrm{e}}(\mathbf{X},t)$ being the first Piola–Kirchhoff stress tensor. $\mathbf{F}_{\mathrm{b}}(\mathbf{X},t)$ represents applied boundary forces such as pericardial forces and tethering forces with details in Sections 2.5 and 2.6. In the current study, the structural strain energy function W takes a general form of

$$W = \bar{W}(\bar{I}_1, I_4) + U(J) \tag{6}$$

where $\bar{I}_1 = J^{-2/3} I_1$, $J = \det(\mathbb{F})$ and $I_1 = \mathrm{trace}(\mathbb{F}^T\mathbb{F})$. $\mathbb{F} = \partial\chi/\partial\mathbf{X}$ represents the deformation gradient tensor. $I_4 = \mathbf{e}\cdot(\mathbb{F}^T\mathbb{F})\mathbf{e}$ denotes the deformation along any preferred direction $\mathbf{e}$ to implement material anisotropy. $U(J)$ is the added volume stabilization term to reinforce the incompressibility constraints following the approach by Vadala-Roth et al. [63] in which

$$U(J) = \frac{\kappa_{\mathrm{stab}}}{2}(\ln J)^2 \tag{7}$$

with $\kappa_{\mathrm{stab}} = 200$ kPa in this study.

2.3. Energy analysis

Two types of energy within heart chambers are investigated: the average kinetic energy (KE)

$$\text{Average KE} = \frac{\int_{\Omega_t^{\mathrm{chamber}}} \frac{1}{2}\rho\mathbf{u}\cdot\mathbf{u}\ \mathrm{d}\mathbf{x}}{\int_{\Omega_t^{\mathrm{chamber}}} \mathrm{d}\mathbf{x}}, \tag{8}$$

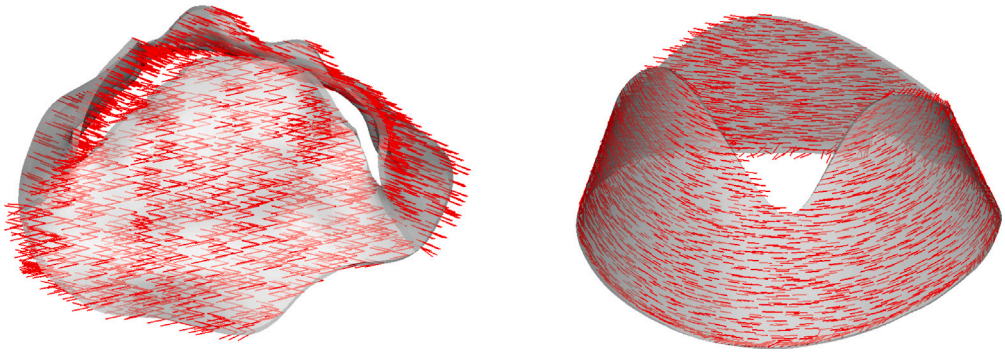

Fig. 8. Mitral and tricuspid valve fibre orientation.

Table 2
Parameter values used for the passive wall material in Eq. (11).

	a (kPa)	b	a_1 (kPa)	b_1	a_2 (kPa)	b_2
Ventricles	0.279	4.033	4.326	10.536	0.894	4.284
Atria	0.279	4.033	4.326	10.536	–	–

and the average energy dissipation rate (EDR)

$$\text{Average EDR} = \frac{\int_{\Omega_t^{\text{chamber}}} \boldsymbol{\Phi} \ \mathrm{d}\mathbf{x}}{\int_{\Omega_t^{\text{chamber}}} \mathrm{d}\mathbf{x}}, \tag{9}$$

in which the energy dissipation function $\boldsymbol{\Phi}$ is defined as

$$\boldsymbol{\Phi} = \mu(\nabla\mathbf{u} + \nabla\mathbf{u}^T) : \nabla\mathbf{u}. \tag{10}$$

2.4. Constitutive modelling

2.4.1. Chamber material

The material properties of the myocardium consist of passive response and active force generation. To model the passive behaviour, an invariant-based, anisotropic constitutive law proposed by Holzapfel and Ogden [21] is used

$$\bar{W}^{\text{passive}} = \frac{a}{2b}\{\exp[b(\bar{I}_1 - 3)] - 1\} + \sum_{i=1}^{\substack{n=1(\text{atrium}) \text{ or} \\ n=2(\text{ventricle})}} \frac{a_i}{2b_i}\{\exp[b_i(I_{4i} - 1)^2] - 1\}, \tag{11}$$

with the stress tensor

$$\begin{aligned}\mathbb{P}^{\text{e}}_{\text{passive}} &= a\exp[b\left(\bar{I}_1 - 3\right)]\left(J^{-2/3}\mathbb{F} - \frac{\bar{I}_1}{3}\mathbb{F}^{-T}\right) \\ &+ \sum_{i=1}^{\substack{n=1(\text{atrium}) \text{ or} \\ n=2(\text{ventricle})}} 2a_i(I_{4i} - 1)\exp\left[b_i\left(I_{4i} - 1\right)^2\right]\mathbb{F}\mathbf{e}_i \otimes \mathbf{e}_i,\end{aligned} \tag{12}$$

where $\mathbf{e}_1$ and $\mathbf{e}_2$ represent the fibre and sheet orientations defined in Section 2.1.5.

The model parameters in Eq. (11) are from the study by Borowska et al. [64] in which cardiovascular magnetic resonance (CMR) scans of healthy volunteers are used for the parameter inference. Table 2 lists all the parameter values.

To account for the atrial and ventricular active contraction, an active stress term is added to the total stress tensor with the form

$$\mathbb{P}^{\text{e}}_{\text{active}} = J\mathrm{T}\mathbb{F}\mathbf{e} \otimes \mathbf{e}, \tag{13}$$

where T denotes the active tension along the fibre direction. Detailed electrophysiology is not included but uniform activation is assumed within ventricles and atria, similar to [32]. Two surrogate models are used to generate the ventricular active tension ($\mathrm{T}_{\text{ventricle}}$) and atrial active tension ($\mathrm{T}_{\text{atrium}}$) respectively. For ventricular active tension, we use the model proposed by Niederer et al. [22] including intracellular calcium transient, calcium binding to Troponin C kinetics, Tropomyosin kinetics, active tension development with crossbridge kinetics. Such a complex model has proven the ability to reproduce realistic contraction behaviours of ventricular myocardium during systole [26,65]. In the current study, all the original model parameters from [22] are kept the same and the resultant active tension is multiplied with a scaling factor (10.5 in LV and 12.0 in RV) to obtain appropriate contractility with an ejection fraction of approximately 50% for both ventricles.

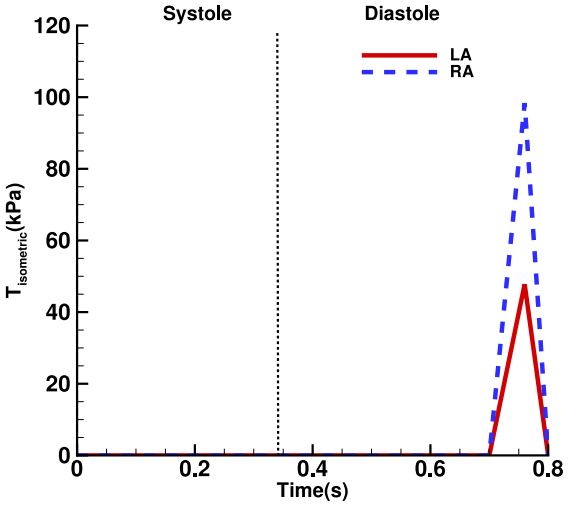

Fig. 9. Prescribed time-varying isometric tension ($T_{isometric}$) along fibre direction for atrial active contraction model in Eq. (14) with peak value 56.2 kPa in left atrium (LA) and 112.4 kPa in right atrium (RA).

Table 3
Parameter values for the valve material model in Eq. (15).

	α (kPa)	β	α_1 (kPa)	β_1	α_2 (kPa)	β_2	κ
MV anterior leaflet	1.640	13.67	11.01	84.85	11.01	84.85	0.08
MV posterior leaflet	0.75	15.00	3.02	144.48	3.02	144.48	0.053
TV leaflets	1.640	13.67	11.01	84.85	–	–	0.08

The atrial contraction lasts approximately one-third of ventricular contraction and in the current model the primary mechanism driving ventricular filling during diastole is not dependent on atrial contraction. Introducing a detailed atrial active tension model would inevitably expand the model's parameter space, especially considering the model's already substantial parameter complexity. Therefore, to ease the model calibration process, we use a simplified atrial active tension model similar to our previous work [34]

$$T_{atrium} = T_{isometric}[1 + \eta(\lambda - 1)], \tag{14}$$

where $T_{isometric}$ is a linear function representing the time-varying isometric tension as shown in Fig. 9 and λ is the stretch along the fibre direction, $\eta = 4.9$. The maximum isometric tension $T^{max}_{isometric}$ is set to assist ventricular end-diastolic filling to reach desired ventricular ejection fractions (approximately 50%).

2.4.2. Valve material

The mitral and tricuspid valve use the same constitutive laws as our previous work [40]

$$\bar{W}^{valve} = \frac{\alpha}{\beta}\{\exp[\beta(\bar{I}_1 - 3)] - 1\} + \sum_{i=1}^{\substack{n=1(TV)\ or\\ n=2(MV)}} \frac{\alpha_i}{2\beta_i}\{\exp[\beta_i(I^*_{4i} - 1)^2] - 1\}, \tag{15}$$

and the stress tensor

$$\begin{aligned}\mathbb{P}^e_{valve} &= 2\alpha\beta\exp[\beta\left(\bar{I}_1 - 3\right)]\left(J^{-2/3}\mathbb{F} - \frac{\bar{I}_1}{3}\mathbb{F}^{-T}\right)\\ &+ \sum_{i=1}^{\substack{n=1(TV)\ or\\ n=2(MV)}} \{2\alpha_i\kappa(I^*_{4i} - 1)\exp\left(\beta_i^{valve}\left(I^*_{4i} - 1\right)^2\right)\mathbb{F}\\ &+ 2\alpha_i(1 - 3\kappa)(I^*_{4i} - 1)\exp\left(\beta_i\left(I^*_{4i} - 1\right)^2\right)\mathbb{F}\mathbf{e}_i \otimes \mathbf{e}_i\}.\end{aligned} \tag{16}$$

where $I^*_{4i} = \max[(\kappa I_1 + (1-3\kappa)I_{4i}), 1]$ and κ is a dispersion parameter [66]. In terms of parameter values, we use the same leaflet and chordae material as our previous work [34] which has proven adequate to capture realistic valve dynamics during cardiac cycles. Table 3 lists all the material parameter values used for mitral and tricuspid valves.

As for the aortic and pulmonary valves, since they are represented by a collection of pseudo fibres, their elastic properties are modelled via a total elastic energy function $E_{valve} = E_{spring} + E_{bending}$ as described in [46]. The Lagrangian force density $\mathbf{F}$ on each fibre is derived as $\mathbf{F} = \mathbf{F}_{spring} + \mathbf{F}_{bending}$. Using the same notation in Section 2.2, let $\mathbf{X} = (X_1, X_2, X_3) \in \Omega_{valve}$ be the Lagrangian

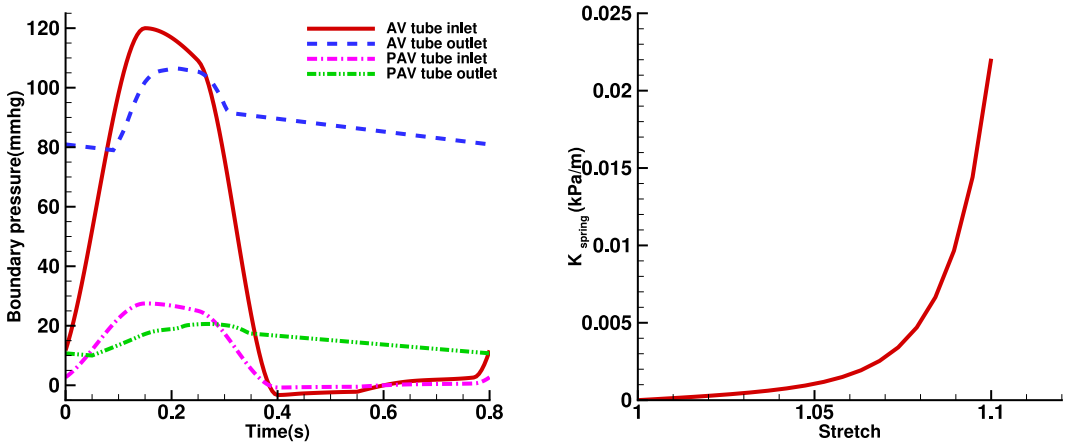

Fig. 10. (Left) Prescribed boundary pressures for the isolated AV/PAV material model test. (Right) Final spring-like force density ($K_{\text{spring}}(l, L)$) used in the AV/PAV material model and the stretch is defined as l/L.

Table 4
Bending stiffness ($c_b(\mathbf{X})$) along radial and circumferential directions for the AV/PAV material model in Eq. (18).

	radial (edge)	radial (belly)	circ. (edge)	circ. (belly)
AV (kPa)	1E+03	5.0	10.0	7.5
PAV (kPa)	1E+03	2.5	2.5	2.5

Table 5
Parameter values for the pericardial traction model in Eq. (19).

	k_p (kPa cm^{-1})	c_p (kPa s cm^{-1})
Atrium	5.0	0.1
Ventricle	1.0	0.1
Transition region	0	0
LV apex region	1.0E+04	0.1

coordinates, in which X_1 and X_2 denote radial and circumferential coordinates respectively, and (X_1, X_2) therefore specifies a particular fibre and X_3 represents the local coordinate on that fibre. The spring-like force density $\mathbf{F}_{\text{spring}}$ is calculated via

$$\mathbf{F}_{\text{spring}} = K_{\text{spring}}(l, L)\, \mathbf{n}_{\text{pseudo-fibre}} \tag{17}$$

where $K_{\text{spring}}(l, L)$ is a force density function depending on the initial fibre length L and current length l. $\mathbf{n}_{\text{pseudo-fibre}}$ is the unit vector along the fibre direction. The bending force density $\mathbf{F}_{\text{bending}}$ is calculated via

$$\mathbf{F}_{\text{bending}} = \frac{\partial^2}{\partial X_3^2}\left(c_b(\mathbf{X})\left(\frac{\partial^2 \chi(\mathbf{X}, t)}{\partial X_3^2} - \frac{\partial^2 \chi(\mathbf{X}, 0)}{\partial X_3^2}\right)\right) \tag{18}$$

where $c_b(\mathbf{X})$ is the bending stiffness specified for each pseudo fibre.

The parameter tuning process for both $\mathbf{F}_{\text{spring}}$ and $\mathbf{F}_{\text{bending}}$ is conducted in isolated valve tests where the valve (AV or PAV) is placed inside a 8 cm long rigid tube with radius 1.5 cm and prescribed boundary pressures mimicking cardiac environment are applied on tube ends as shown in Fig. 10(Left). For $\mathbf{F}_{\text{spring}}$, we first fit the experimental data from Koch et al. [67] who conducted uniaxial tensile tests on fresh porcine aortic valve leaflets, using the same constitutive law as Eq. (15), and re-scale the fitted parameters to allow approximately 90 mL of transvalvular flow during valve opening. Fig. 10(Right) shows the plot of $K_{\text{spring}}(l, L)$ used in the current study. As for $c_b(\mathbf{X})$, our test results show that the bending stiffness plays an important role in maintaining valve closure shape. To withstand typical pressure load (80 mmHg for AV and 5 mmHg for PAV) during valve closure and minimize the negative impact of high bending stiffness on valve opening, inhomogeneous bending stiffness $\mathbf{F}_{\text{bending}}$ is used as shown in Table 4. Finally, Fig. 11 plots the transvalvular flow rate for both valves under the aforementioned test conditions to demonstrate the valve function with the current parameter settings.

2.5. Boundary conditions

Fig. 12 shows the complete heart model with valves included. The artificial venous vessels remain rigid whereas the arterial vessels are defined with elastic properties to allow deformation in order to assist the movement of the atrioventricular plane. The

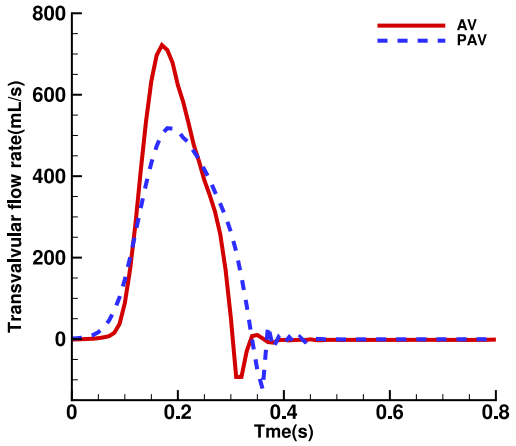

Fig. 11. Transvalvular flow results in the isolated AV/PAV material model test. Total cardiac output is 89 mL for AV and 87 mL for PAV during one cardiac cycle.

Table 6
Parameter values used in the three-element Windkessel model at arterial vessel outlet.

	Peripheral resistance (R) (mmHg s mL^{-1})	Compliance (C) (mL $mmHg^{-1}$)	Characteristic impedance (Z_c) (mmHg s mL^{-1})
Aorta outlet	0.68	3.42	0.03
Pulmonary artery outlet	0.08	27.41	0.005

left ventricular apex is defined as a circular region on the epicardial surface with a radius of 0.5 cm (Fig. 12(Right)). The pericardium-heart interactions are simulated via applied traction on the epicardial surfaces. Following the study by Pfaller et al. [68], the traction model consisting of a spring and a dashpot in parallel takes the form

$$\mathbf{T}_{\text{epi}}(\mathbf{X},t) = \{k_p[\chi(\mathbf{X},t) - \chi(\mathbf{X},t_{\text{ref}})] \cdot \mathbf{N}_{\text{ref}} - c_p[\dot{\overline{\chi(\mathbf{X},t) - \chi(\mathbf{X},t_{\text{ref}})}}] \cdot \mathbf{N}_{\text{ref}}\}\mathbf{N}_{\text{ref}}. \tag{19}$$

The reference configuration for the heart is chosen to be at diastasis (t_{ref}) when all chambers are at rest prior to atrial contraction. $\mathbf{N}_{\text{ref}}$ is the unit vector perpendicular to heart epicardial surfaces. Notice that the traction is applied on the entire epicardial surface except a transition region as shown in Fig. 12(Right) to account for the epicardial adipose tissue [18]. Table 5 lists parameter values for the traction model. Finally, to set up a closed system, prescribed pressures are applied to the entries of the venous vessels as shown in Fig. 13 and three-element Windkessel models [69] are applied to the outlet of arterial vessels with parameter values shown in Table 6.

2.6. Simulation design

The current study aims to develop a whole-heart model with the focus on fluid–structure interactions. Three key cardiac phenomena are of interest: the interactions between valve leaflet and surrounding flow, the effect of the movement of atrioventricular plane and pericardium-heart interactions. Therefore numerical simulations are designed to demonstrate the advantages of such complex model in capturing these phenomena and revealing more insights of the overall heart function. Three cases are designed as follows

1. $\mathbf{WH_{Rigid}}$ (the whole heart model with rigid annulus): here we apply commonly used simplified boundary conditions including fixed arteries and fixed valve annulus using tethering force

$$\mathbf{F}_{\text{b}}(\mathbf{X},t) = \begin{cases} \gamma(\mathbf{X}-\mathbf{x}) & , \mathbf{X} \in \partial\Omega^{\text{s}}_{\substack{\text{annulus or}\\ \text{arteries}}} \\ 0 & , \text{otherwise} \end{cases} \tag{20}$$

   and γ = 2.5E+04 kpa. As a result, the left and right atrioventricular planes (LAVP and RAVP) remain fixed throughout the cardiac cycle. The LV apex is left free to allow sufficient ventricular pumping.
2. $\mathbf{WH_{Free}}$ (the whole heart model with free annulus): all valve annulus are left free to move with elastic arterial vessels. Since no restrictions are applied around the atrioventricular plane, we fix LV apex to stabilize the heart motion where

$$\mathbf{F}_{\text{b}}(\mathbf{X},t) = \begin{cases} \gamma(\mathbf{X}-\mathbf{x}) & , \mathbf{X} \in \partial\Omega^{\text{s}}_{\text{LV apex region}} \\ 0 & , \text{otherwise} \end{cases} \tag{21}$$

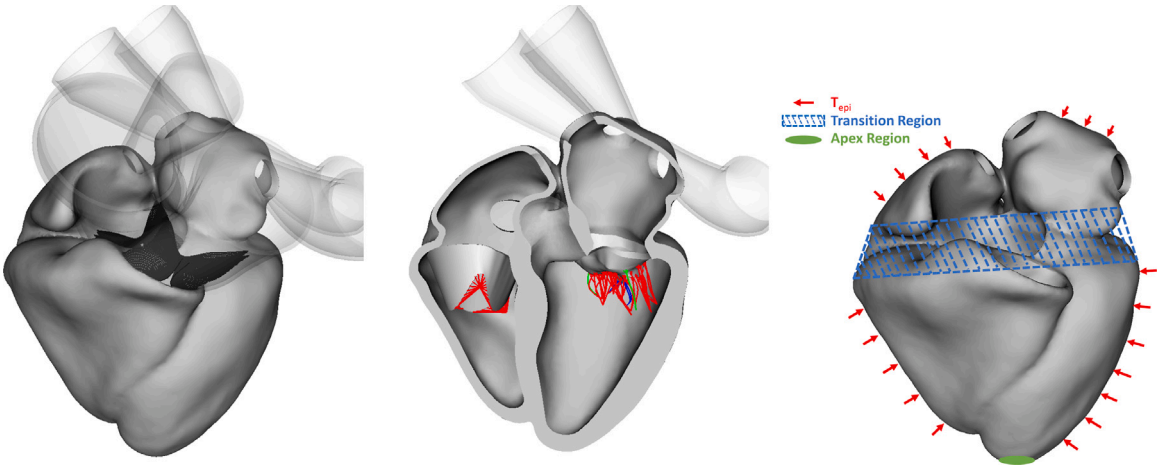

Fig. 12. (Left and Mid) Complete whole-heart model with all valves and artificial vessels. (Right) Illustration of added pericardial traction: red arrows show regions where pericardial traction is applied, blue shaded region is the transition region with zero traction and the green region is the LV apex region. (For interpretation of the references to colour in this figure legend, the reader is referred to the web version of this article.)

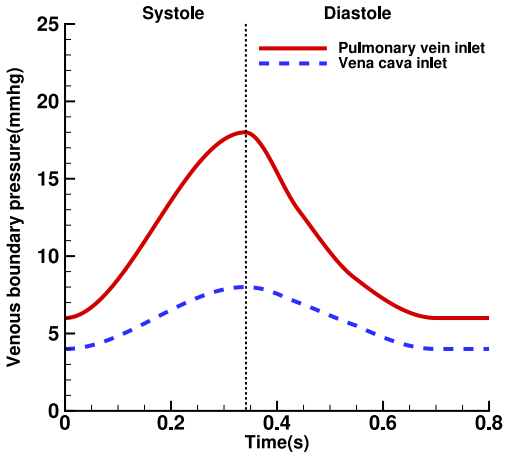

Fig. 13. Prescribed pressures at pulmonary vein vessel inlet and vena cava vessel inlet.

3. $\mathbf{WH_{Peri}}$ (the whole heart model with pericardial force applied): free valve annulus with elastic arteries similar to $\mathbf{WH_{Free}}$, and applied pericardial boundary traction (Eq. (19)) on heart epicardial surfaces as shown in Fig. 12(Right). Therefore

$$\mathbf{F}_{\mathrm{b}}(\mathbf{X},t)=\begin{cases}\mathbf{T}_{\mathrm{epi}}(\mathbf{X},t) & ,\ \mathbf{X}\in\partial\Omega^{\mathrm{s}}_{\text{epicardial surface}}\\ 0 & ,\ \text{otherwise}\end{cases} \tag{22}$$

The whole-heart model is immersed in viscous fluid with density $1.0\times10^{3}\,\mathrm{kg\,m^{-3}}$ and dynamic viscosity $4.0\times10^{-3}\,\mathrm{kg\,m^{-1}\,s^{-1}}$. The fluid mesh has the grid spacing 0.1 cm × 0.1 cm × 0.1 cm, and the heart geometry is discretized with a tetrahedral mesh with the average element edge length 0.125 cm in chambers and 0.05 cm in valves. The timestep size is 5.0×10^{-6} s. All simulations are run on ARCHER2 (http://www.archer2.ac.uk), an HPE Cray EX supercomputing system. One cardiac cycle takes about 72 h in wall-clock time on four AMD EPYCTM 7742 (64-core, 2.25 GHz) processors. For each simulation, multiple cardiac cycles are run before converging to a steady state, usually at the third cycle.

3. Results

This section provides a comprehensive overview of the numerical results across all three cases. We begin by showcasing the deformation of the heart in Fig. 14 with a demonstration of atrioventricular plane movement (Fig. 15), and quantitative comparisons for MV/TV annular dynamics (Fig. 16). We then show the simulated pressure and volume for heart chambers in Figs. 17 and 18

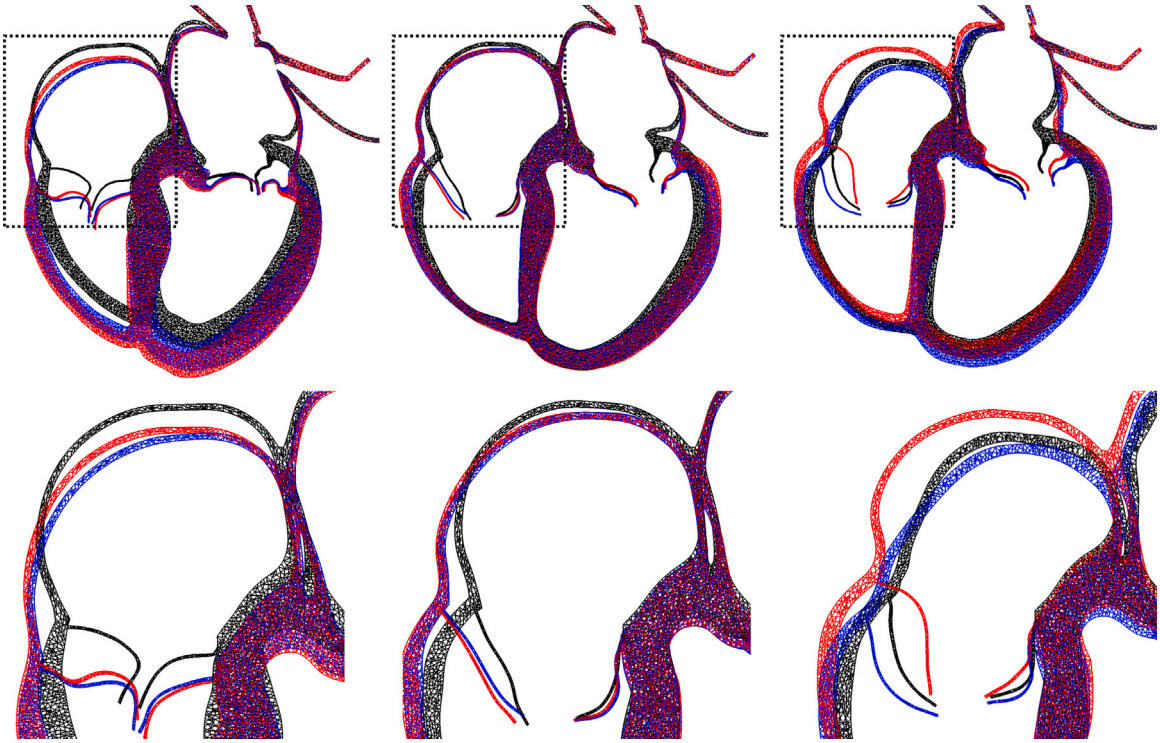

Fig. 14. Heart deformation in four-chamber view at (Top left) end-systole (0.34 s), (Top mid) mid diastole (0.7 s) and (Top right) end-diastole (0.8 s) for $\mathbf{WH_{Rigid}}$ in black, $\mathbf{WH_{Free}}$ in blue and $\mathbf{WH_{Peri}}$ in red. (Bottom row) Corresponding zoom-in view of the square region to show the right atrioventricular plane movement and the effect of added pericardial forces on preventing the RA free wall from collapsing during atrial contraction. (For interpretation of the references to colour in this figure legend, the reader is referred to the web version of this article.)

with the pressure-volume loops in Fig. 19. Next, we describe the flow field inside heart chambers in Fig. 20 and near valve leaflets in Figs. 21 and 22. Quantitative comparisons of venous flow and transvalvular flow are summarized in Figs. 23 and 24. Finally, we finish this section by discussing the kinetic energy and energy dissipation within heart chambers in Fig. 25.

Fig. 14 shows heart deformation in four-chamber view at end-systole, mid diastole and end-diastole. The movement of atrioventricular planes throughout the cardiac cycle is captured and overall, the right atrioventricular plane (RAVP) presents larger displacement along the longitudinal axis (perpendicular to the atrioventricular plane) compared to the left atrioventricular plane (LAVP). In cases of $\mathbf{WH_{Free}}$ and $\mathbf{WH_{Peri}}$, the ventricular contraction causes atrioventricular planes to move towards fixed apex during systole and immediately spring back during ventricular rapid filling at early diastole. During late diastole, atria pull atrioventricular planes further away from the apex to assist atrial active emptying. On the other hand, $\mathbf{WH_{Rigid}}$ achieves ventricular emptying and filling by allowing free apex to move towards the ventricular base during systole and away during diastole. Another important thing to notice is the deformation of atrial-free walls especially for the right atrium. At late diastole, the free walls in both $\mathbf{WH_{Rigid}}$ and $\mathbf{WH_{Free}}$ collapse inwards as a result of atrial contraction shown in Fig. 14 (Right), whereas $\mathbf{WH_{Peri}}$ achieves atrial contraction by larger atrioventricular plane displacement as a compensation to restricted free wall deformation due to applied pericardial forces.

Fig. 15 further demonstrates the atrioventricular plane movement in $\mathbf{WH_{Peri}}$ throughout the cardiac cycle. The RAVP and LAVP reference locations (broken lines) are chosen at mid-diastole prior to atrial contraction. In comparison, we also show atrioventricular plane movement captured in a Magnetic Resonance Imaging (MRI) dataset from a healthy volunteer with a reference location defined in the same fashion. Similarities in RAVP and LAVP movement can be seen between our simulation results and the MRI scan.

Fig. 16(Top row) plot quantitative measurements of LAVP and RAVP displacement along the longitudinal axis with reference location obtained prior to atrial contraction. Negative displacement indicates movement towards the apex. The plane movement observed in Fig. 15 is reflected here. The fast decrease at early systole corresponds to ventricle-pulling motion, and the fast increase at early diastole corresponds to LAVP/RAVP springing back at the ventricular fast-filling stage. The atrial contraction leads to a further increase at late diastole. Besides the movement along the longitudinal axis, the MV and TV annulus also experience compression during systole and expansion during diastole. Fig. 16(Bottom row) show the change of valve annulus width which is defined to be the distance between the mid-anterior annulus and mid-posterior annulus for MV, and the distance between mid-septal annulus and anterior-posterior commissure for TV. This annulus width parameter reflects the annulus orifice area change during the cardiac cycle, and it is interesting to see a biphasic pattern especially in $\mathbf{WH_{Peri}}$ with a first wave in early systole caused by rapid ventricular pressure increase prior to arterial valves (AV and PAV) opening, and a second wave during diastole due to ventricular filling.

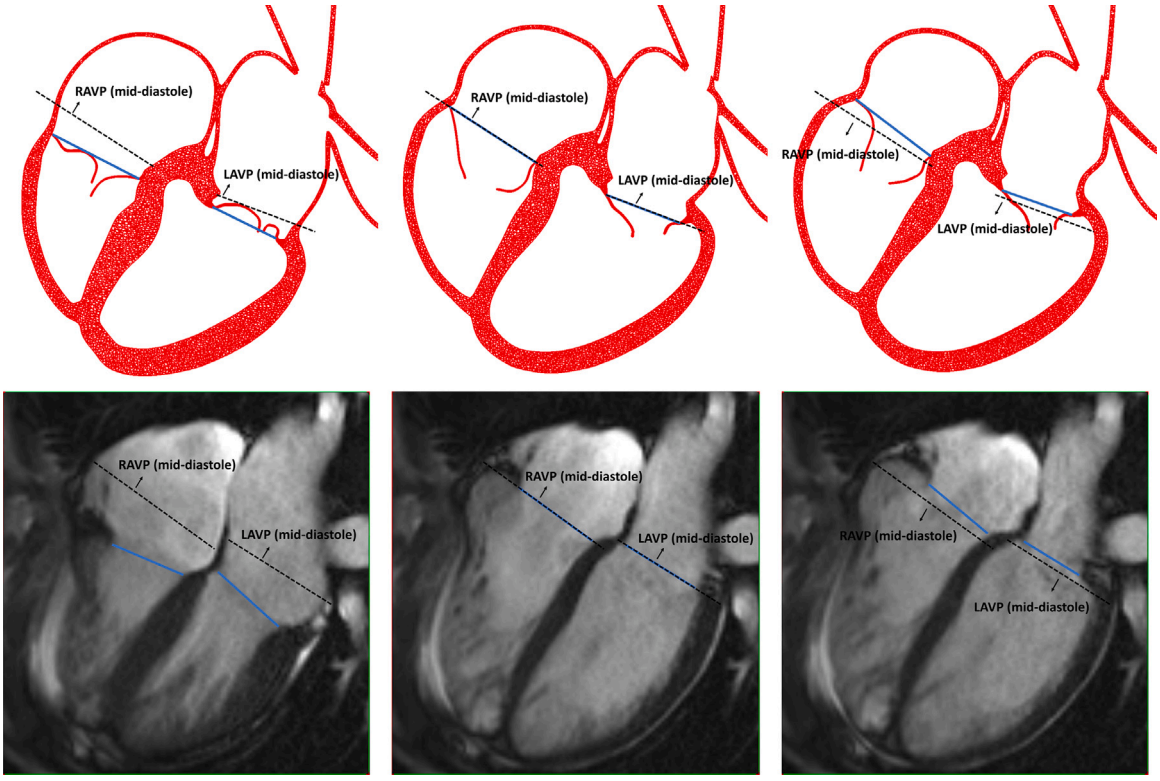

Fig. 15. Illustration of left and right atrioventricular plane (LAVP/RAVP) movement in $\mathbf{WH_{Peri}}$ at (Top left) end-systole (0.34 s), (Top mid) mid diastole (0.7 s) and (Top right) end-diastole (0.8 s). Blue solid lines represent the detected LAVP and RAVP locations. The reference plane location is chosen at mid-diastole prior to atrial contraction which is shown in broken lines. In comparison, atrioventricular plane movement is captured in MRI scans from a healthy volunteer at (Bottom left) end-systole, (Bottom mid) mid diastole and (Bottom right) end-diastole. Similarly, the reference location is chosen at mid-diastole. (For interpretation of the references to colour in this figure legend, the reader is referred to the web version of this article.)

Fig. 17 shows simulated fluid pressure in each chamber. In ventricles, the added pericardial forces in $\mathbf{WH_{Peri}}$ reduce systolic pressure compared with $\mathbf{WH_{Rigid}}$ and $\mathbf{WH_{Free}}$ under the same boundary conditions. Between left and right ventricles, RV pressure drops almost immediately after reaching the peak whereas the LV pressure is withheld for a short period at the peak, which is primarily due to the different resistance and compliance imposed at downstream Windkessel models. Also, the unphysiological RV pressure plateau at end-systole suggests the need for improvement in ventricular active contraction modelling. For atrial pressure, typical A wave and V wave are seen and all three cases reach the same end systolic pressure after filling because of the same venous pressure boundary conditions. However, the filling process during systole presents different behaviours across three cases, especially in the right atrium where significant valve movement is observed as shown in Fig. 16. For example, $\mathbf{WH_{Rigid}}$ has a steady pressure increase during filling under the sole influence of prescribed upstream pressure boundary conditions. when pericardial forces are absent, $\mathbf{WH_{Free}}$ experiences a sudden pressure increase at early systole, which is caused by RAVP moving towards the fixed apex (Fig. 16(Top right)) and such movement compresses the RA chamber leading to reduced systolic inflow from vena cava. However, after adding pericardial forces to restrict the RA-free wall motion, this compression phenomenon disappears and the RAVP movement creates a vacuum effect instead which leads to low RA pressure at early systole and large systolic inflow from vena cava as shown in Fig. 23. The large mid-systole RA pressure wave in $\mathbf{WH_{Peri}}$ is a result of this improved filling process. During diastole, all three cases present similar pressure patterns and a refilling diastolic wave is observed in LA.

Fig. 18 plots the normalized chamber volume throughout the cardiac cycle. In ventricles, fast volume change happens during systole after AV/PAV opens, early diastole after MV/TV opens and late diastole due to atrial contraction. The atrial volume change in $\mathbf{WH_{Free}}$ and $\mathbf{WH_{Peri}}$ suggest the majority of the atrial filling is conducted at early systole. Also, the effect of free annular dynamics is seen at early diastole with faster ventricular filling and atrial emptying in $\mathbf{WH_{Free}}$ and $\mathbf{WH_{Peri}}$ compared with the fixed annulus in $\mathbf{WH_{Rigid}}$. Fig. 19 plots pressure-volume loop for ventricles and atria in $\mathbf{WH_{Peri}}$. Notice that ventricular PV loops have the same slope during diastole due to the same passive material and during systole, LV has a more square-shaped PV loop compared to RV which is caused by the differences in the downstream Windkessel models. The sharp gradient at the end-systole is caused by the artificial boundary conditions to enforce the linear decay of ventricular active tension towards zero by the end of isorelaxation. On the other hand, atrial PV loops show very different slopes during filling. RA seems more compliant than LA even though the same passive material is used for both. This suggests that besides wall material, other factors such as constraints imposed by venous vessels and atrioventricular plane movement also contribute to overall atrial compliance. Another important note is that the typical

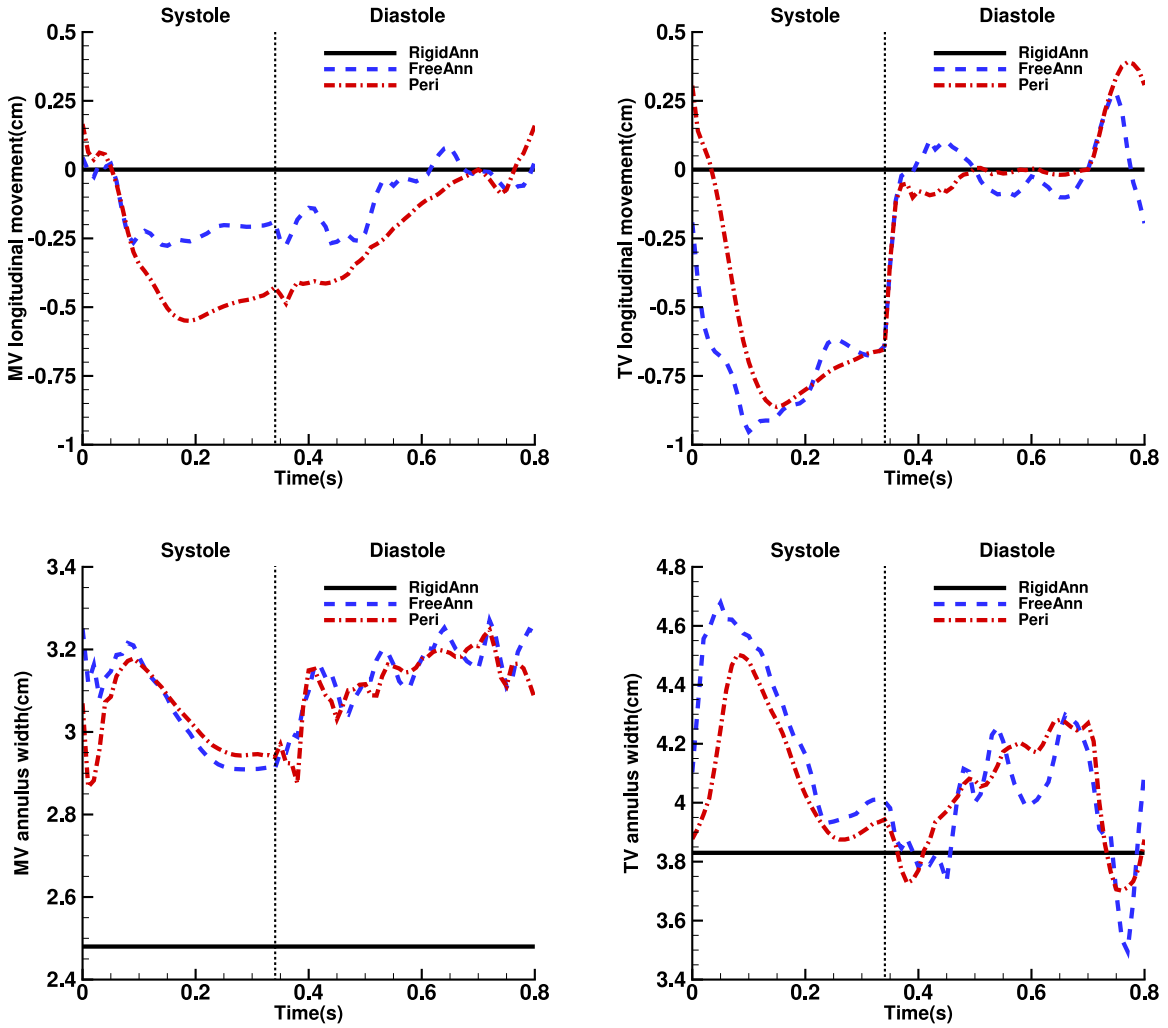

Fig. 16. The longitudinal movement of MV (Top left) and TV annulus (Top right) during the cardiac cycle in $\mathbf{WH}_{\mathbf{Rigid}}$, $\mathbf{WH}_{\mathbf{Free}}$ and $\mathbf{WH}_{\mathbf{Peri}}$. The MV and TV annulus width change are plotted in the bottom row.

A loop caused by atrial contraction is present but the V loop caused by atrial filling and passive emptying is not captured in the current model. As a result, the typical figure-8 pattern for the atrial PV loop is not observed in our results. The possible causes include atrial passive material modelling, prescribed venous pressure and fixed venous vessels which all affect the atrial filling and passive emptying process.

Fig. 20(Top row) shows MV and TV transvalvular flow patterns throughout the cardiac cycle in $\mathbf{WH}_{\mathbf{Peri}}$. At early diastole, MV flow jets shoot towards the LV posterior lateral wall before reaching the LV apex, and then move towards the LV base creating large clockwise vortices as shown in Fig. 20(Bottom left). On the other hand, TV flow jets orient directly towards the RV apex, therefore no similar vortices are observed in RV. Besides these large vortices, small vortex rings near valve-free edges can be detected using the so-called Lambda2 method. In details, let $\mathbb{V}$ be a tensor

$$\mathbb{V} = \left(\frac{\nabla\mathbf{u} + \nabla\mathbf{u}^{\top}}{2}\right)^2 + \left(\frac{\nabla\mathbf{u} - \nabla\mathbf{u}^{\top}}{2}\right)^2 \tag{23}$$

with eigenvalues $\lambda_1 \geq \lambda_2 \geq \lambda_3$ and fluid regions with $\lambda_2 \leq 0$ indicate vortex core. By choosing the appropriate threshold value for the λ_2 contour plot, vortex rings near MV and TV can be seen at early systole and during atrial contraction as shown in Fig. 20(Bottom mid and right). Inflow waves from pulmonary veins and vena cava are also demonstrated. Besides flow patterns, energy dissipation function Φ defined in Eq. (10) is also plotted in the middle row for early systole, early diastole and late diastole. As expected, a high energy dissipation rate is found close to the fluid–structure interface such as the atrial side of MV and TV leaflets during opening, and also near transvalvular flow jets inside ventricles.

A three-chamber view of the AV transvalvular flow field is in Fig. 21(Left and mid) showing large outflow jets during systole with the peak transvalvular flow velocity 263.3 cm/s. The vortex formation is also observed downstream close to the left coronary

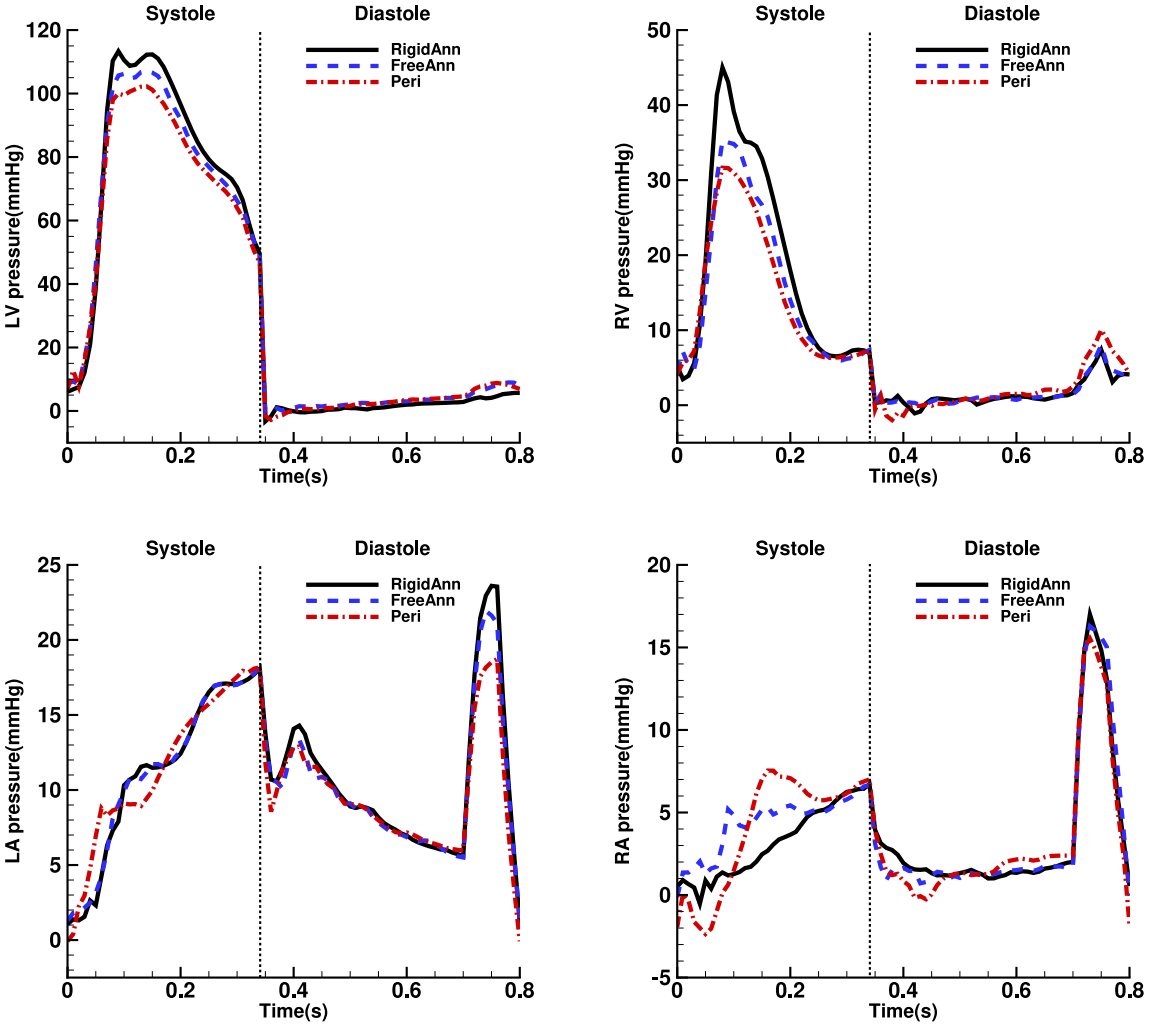

Fig. 17. Fluid pressure in (Top left) LV, (Top right) RV, (Bottom left) LA and (Bottom right) RA for all three cases.

leaflet (cusp) as shown in Fig. 21(Right). To further demonstrate the effect of AV leaflets on the surrounding flow, a cross-section view of the aorta at approximately 1 cm downstream to AV leaflets is shown in Fig. 22 with the corresponding AV shapes during valve opening and closing. PAV and AV transvalvular flow share similar patterns in the current model, it is not shown here to avoid repetition. Also, in general, $\mathbf{WH_{Rigid}}$ and $\mathbf{WH_{Free}}$ present similar vortex patterns within ventricles compared with $\mathbf{WH_{Peri}}$.

Fig. 23 plots the flow rate at superior pulmonary veins and vena cava. A biphasic flow pattern is seen with an early systolic wave (S wave) and an early diastolic wave (D wave). The atrial contraction at late diastole suppresses venous inflow due to increased chamber pressure. For pulmonary venous flow, $\mathbf{WH_{Rigid}}$ and $\mathbf{WH_{Free}}$ present similar flow profile whereas $\mathbf{WH_{Peri}}$ introduces a slightly earlier S wave. With larger atrioventricular movement in the right heart, flow at the vena cava shows more different behaviours among the three cases, especially during systole (atrial filling). For example, $\mathbf{WH_{Free}}$ shows reduced S wave compared to $\mathbf{WH_{Rigid}}$ as a result of the sudden pressure increase at early systole in RA due to aforementioned chamber compression (Fig. 17(Bottom right)). On the other hand, since $\mathbf{WH_{Peri}}$ has the lowest RA pressure at early systole due to the vacuum effect as shown in Fig. 17(Bottom right), a significantly increased S wave appears indicating faster early systole filling.

Fig. 24 shows the transvalvular flow rate at all four valves. All three cases have similar flow profiles such as a single systolic wave for AV and PAV, and early and late diastolic waves for MV and TV (known as the E wave and A wave). Stroke volume can be calculated via flow rate integration at AV and PAV as shown in Tables 7, and 8 lists all wave peak values. It is interesting to note that both $\mathbf{WH_{Free}}$ and $\mathbf{WH_{Peri}}$ have a larger MV E wave compared to $\mathbf{WH_{Rigid}}$, indicating faster ventricular filling and atrial emptying as expected. However, the TV E wave does not follow the same pattern among the three cases and $\mathbf{WH_{Rigid}}$ actually produces the highest peak. To investigate, we calculate the ventricular volume increase at early diastole (from valve opening to post E wave) as shown in Table 9, which should accurately reflect early diastole filling in ventricles. It can be seen that both $\mathbf{WH_{Free}}$ and $\mathbf{WH_{Peri}}$ have larger LV volume increase which agrees with the MV E wave profile in Fig. 24(Bottom left). However,

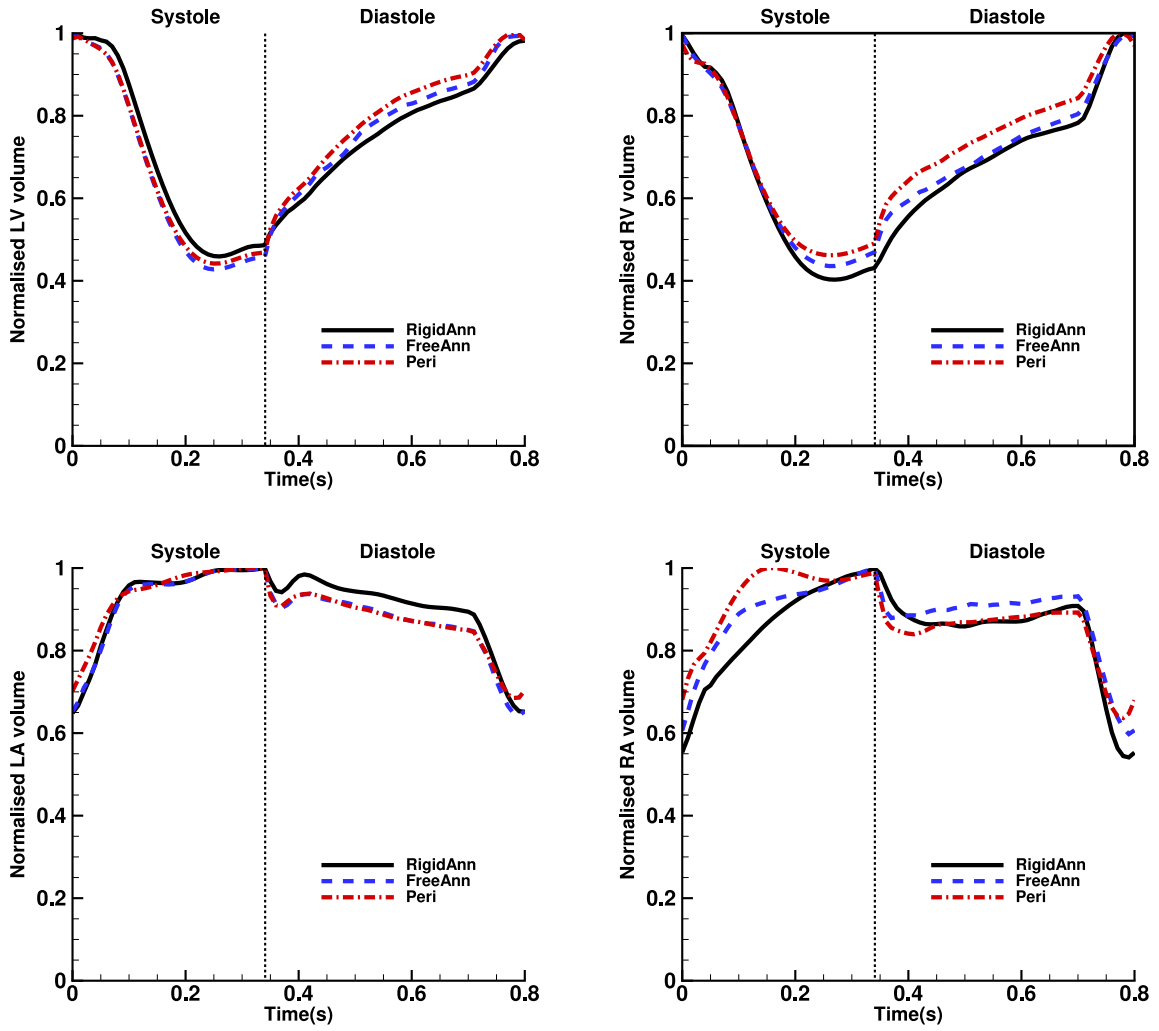

Fig. 18. Normalized cavity volume in (Top left) LV, (Top right) RV, (Bottom left) LA and (Bottom right) RA for all three cases. Volume for each chamber is normalized against its maximum volume during the cardiac cycle.

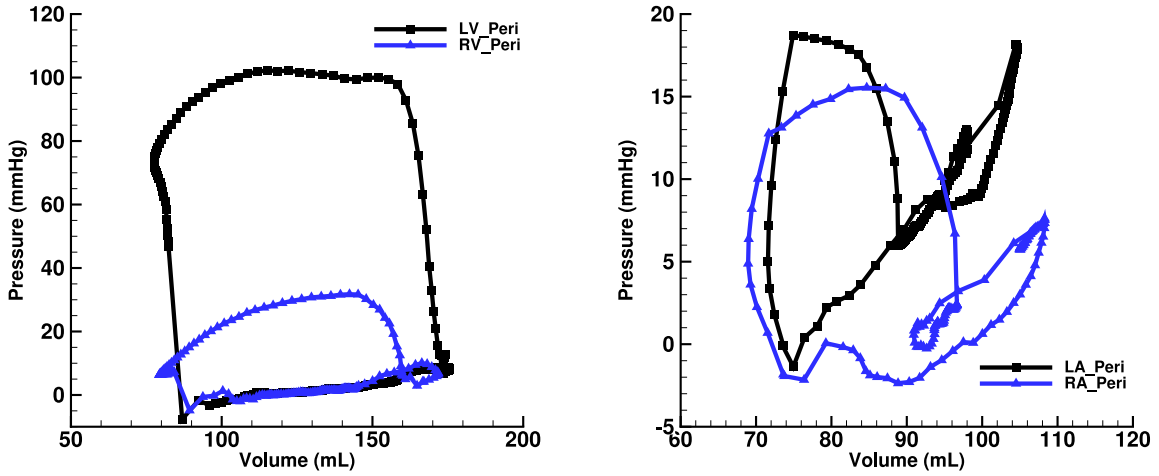

Fig. 19. Pressure-volume loop for (Left) ventricles and (Right) atria in $\mathbf{WH}_{\mathbf{Peri}}$. The 'square' and 'triangle' symbols represent outputted data points with a time interval of 0.005 s.

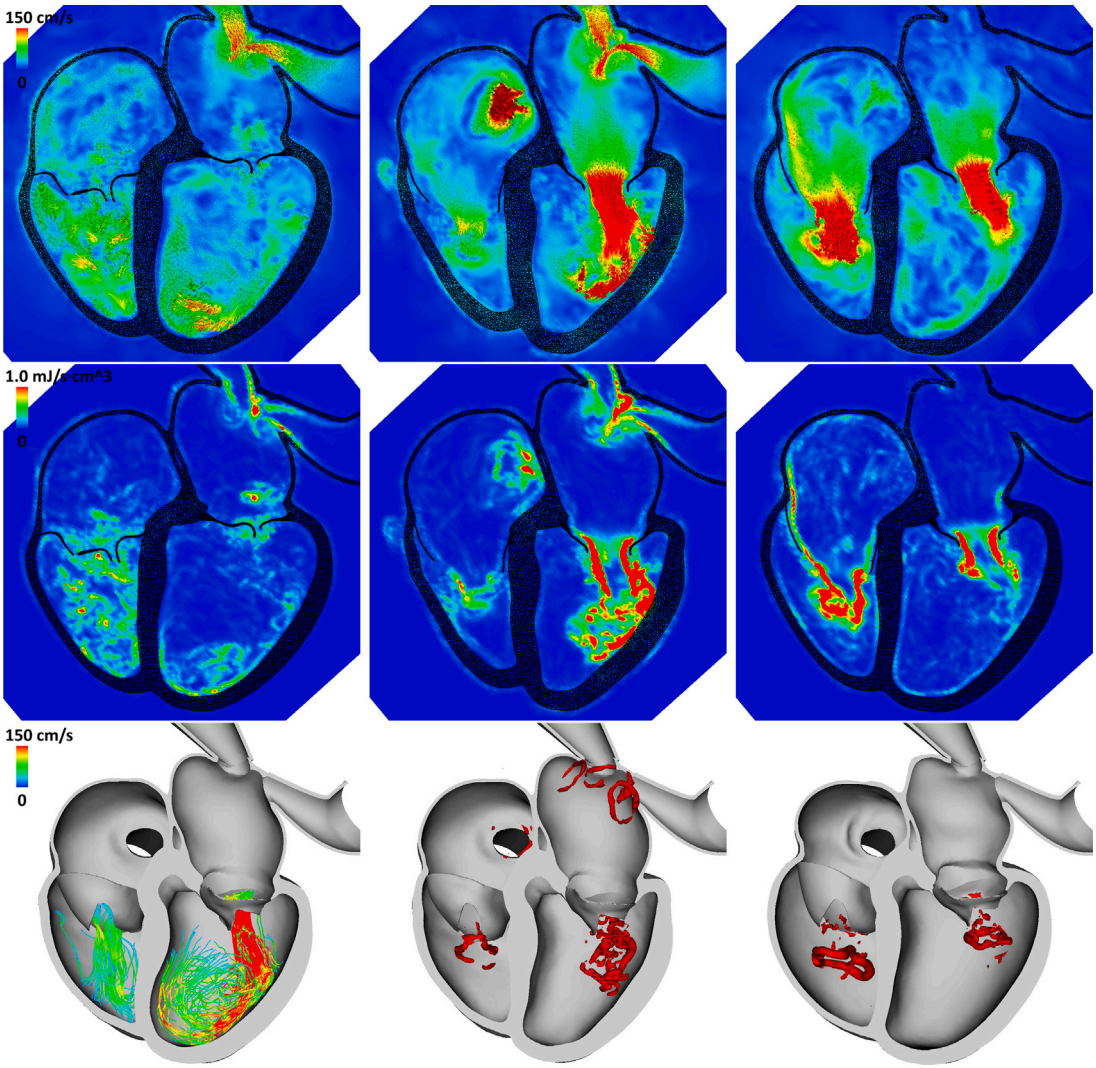

Fig. 20. Fluid velocity with vector (coloured in magnitude) in four-chamber view at (Top left) early systole (0.05 s), (Top mid) early diastole (0.4 s) and (Top right) late diastole (0.75 s) in $\mathbf{WH}_{\mathbf{Peri}}$. At the same time points, the energy dissipation function (Φ) is plotted at (Middle left) early systole, (Middle centre) early diastole and (Middle right) late diastole. (Bottom left) Transvalvular flow streamlines near MV and TV (coloured in velocity magnitude) at early diastole (0.5 s) and vortex rings detected using the so-called Lambda2 method at (Bottom mid) early diastole (0.4 s) and (Bottom right) late diastole (0.75 s). (For interpretation of the references to colour in this figure legend, the reader is referred to the web version of this article.)

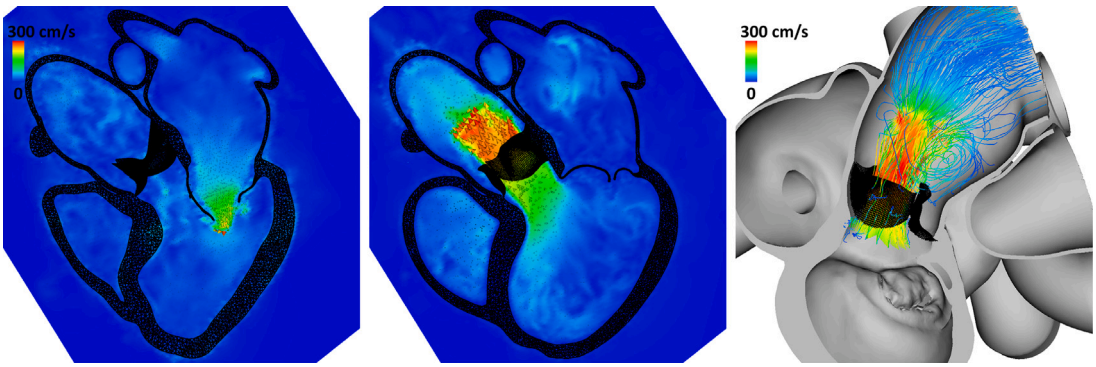

Fig. 21. Fluid velocity with vector (coloured in magnitude) in three-chamber view at (Left) early diastole (0.36 s) and (Mid) early systole (0.11 s) in $\mathbf{WH}_{\mathbf{Peri}}$. (Right) Transvalvular flow streamlines near AV (coloured in velocity magnitude) at early systole (0.11 s). (For interpretation of the references to colour in this figure legend, the reader is referred to the web version of this article.)

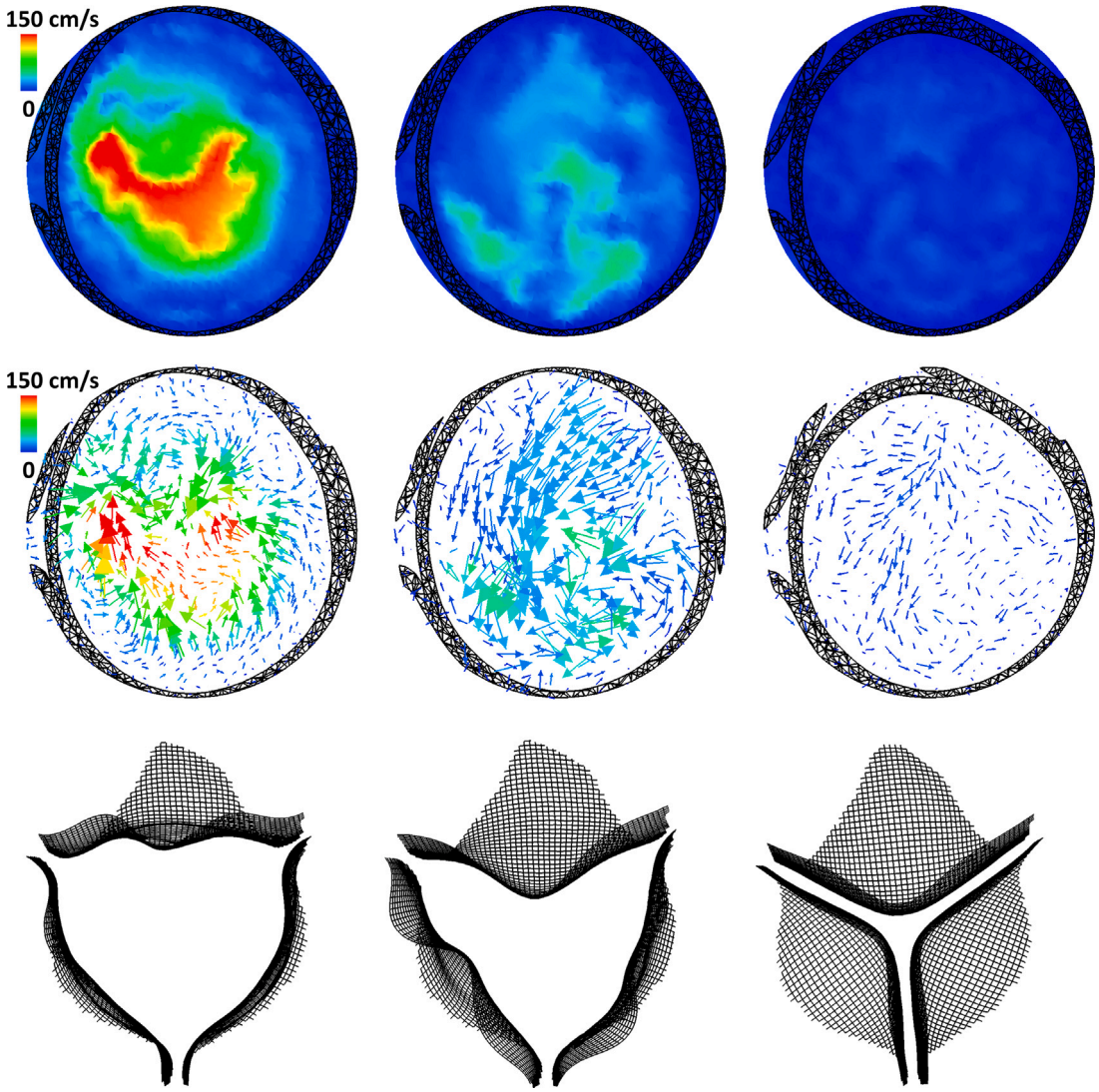

Fig. 22. Fluid velocity with vector (coloured in magnitude) in the cross-section view of ascending aorta at approximately 1 cm downstream to AV, and the corresponding AV deformation at (Left column) early systole (0.11 s), (Mid column) mid systole (0.19 s), (Right column) early diastole (0.5 s) in $\mathbf{WH_{Peri}}$. (For interpretation of the references to colour in this figure legend, the reader is referred to the web version of this article.)

in the case of RV, $\mathbf{WH_{Peri}}$ presents the largest volume increase during early diastole which contradicts the TV E wave profile in Fig. 24(Bottom right). Combining the atrioventricular plane movement shown in Fig. 16, we speculate that this is because the flow rate is currently integrated on a fixed plane at the valve orifice. When fast atrioventricular movement along the longitudinal axis is present, the integration plane velocity should also be considered and this will be addressed in future models.

Fig. 25 shows the average kinetic energy (KE) and average energy dissipation rate (EDR) within both atria and ventricles. All three cases present triple KE waves during the cardiac cycle with one systolic wave corresponding to atrial filling and ventricular ejection, one early diastolic wave corresponding to atrial conduit phase and ventricular rapid filling, and one late diastolic wave corresponding to atrial contraction. However, there are still noticeable differences among these cases. For example, since the average KE directly reflects the magnitude of fluid velocity, the free annular dynamics lead to faster atrial flow during the conduit phase with an enhanced early diastole KE wave in atria. Interestingly, during atrial active contraction, $\mathbf{WH_{Peri}}$ has the smallest late diastole KE wave among three cases in both atria and ventricles, which suggests the two mechanisms involved in the atrial active emptying process: the first mechanism is via atria squeezing out blood into ventricles with increased fluid velocity and the second mechanism is via atrioventricular plane moving away from apex which does not speed up the blood flow. In terms of the energy dissipation rate, high KE usually leads to high EDR as suggested in the plot. Therefore, the significantly reduced late diastole KE wave in $\mathbf{WH_{Peri}}$ also leads to less energy dissipation especially inside ventricles during atrial contraction.

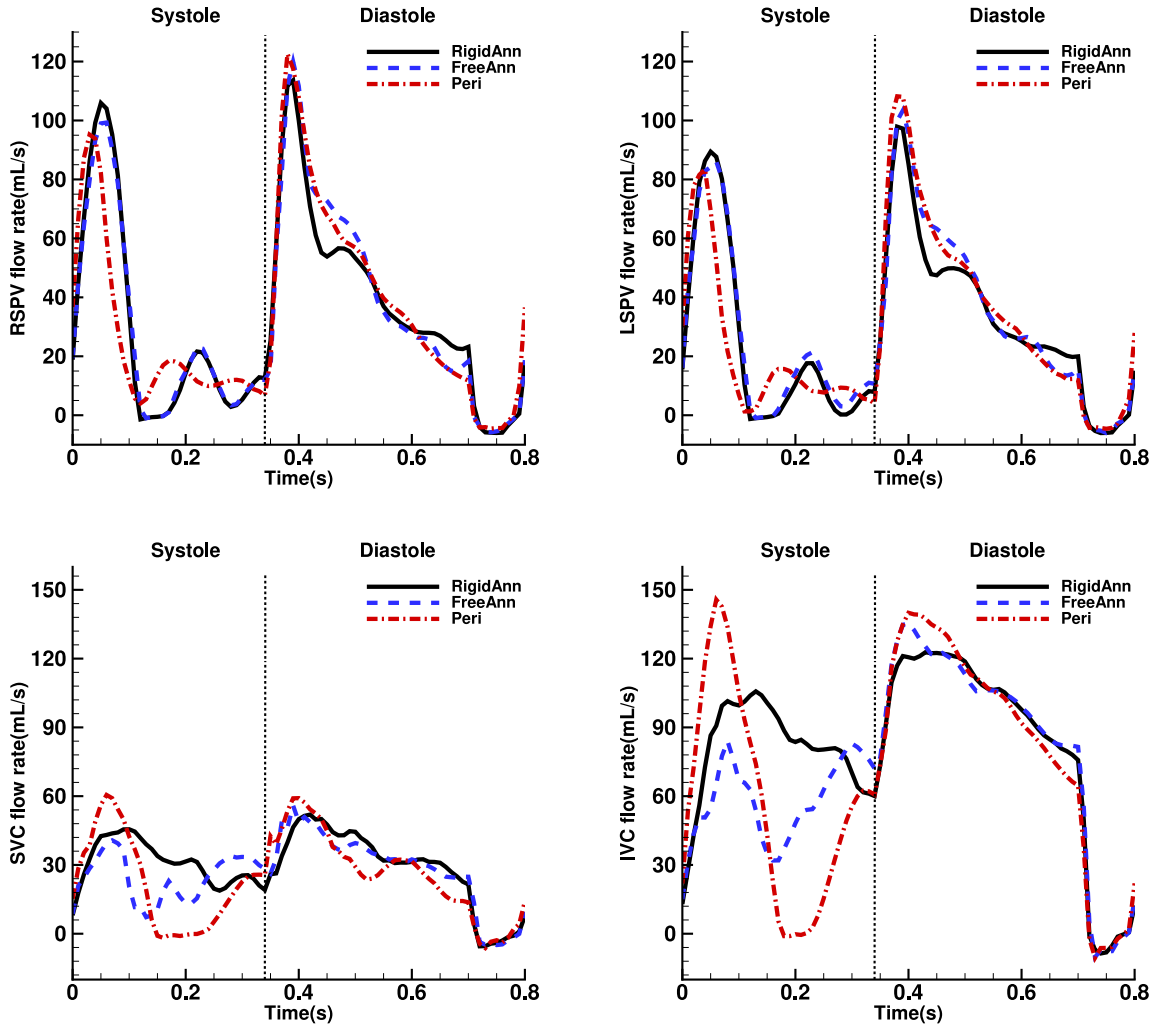

Fig. 23. Flow rate at vessel inlet of (Top left) right superior pulmonary vein, (Top right) left superior pulmonary vein, (Bottom left) superior vena cava and (Bottom right) inferior vena cava in all cases.

Table 7
Ventricle stroke volume and ejection fractions.

	WH_{Rigid}	WH_{Free}	WH_{Peri}
LV stroke volume	87.5 mL	90.8 mL	84.1 mL
LV ejection fraction	51.7%	50.9%	48.5%
RV stroke volume	91.7 mL	82.0 mL	77.1 mL
RV ejection fraction	53.2%	47.2%	46.2%

Table 8
Transvalvular flow rate peaks (mL/s).

	WH_{Rigid}	WH_{Free}	WH_{Peri}
AV (systolic wave)	756.2	812.9	747.3
PAV (systolic wave)	773.1	701.8	623.6
MV (E wave)	411.9	575.3	587.6
MV (A wave)	314.7	389.7	297.3
TV (E wave)	468.3	351.6	453.5
TV (A wave)	654.7	531.1	450.1

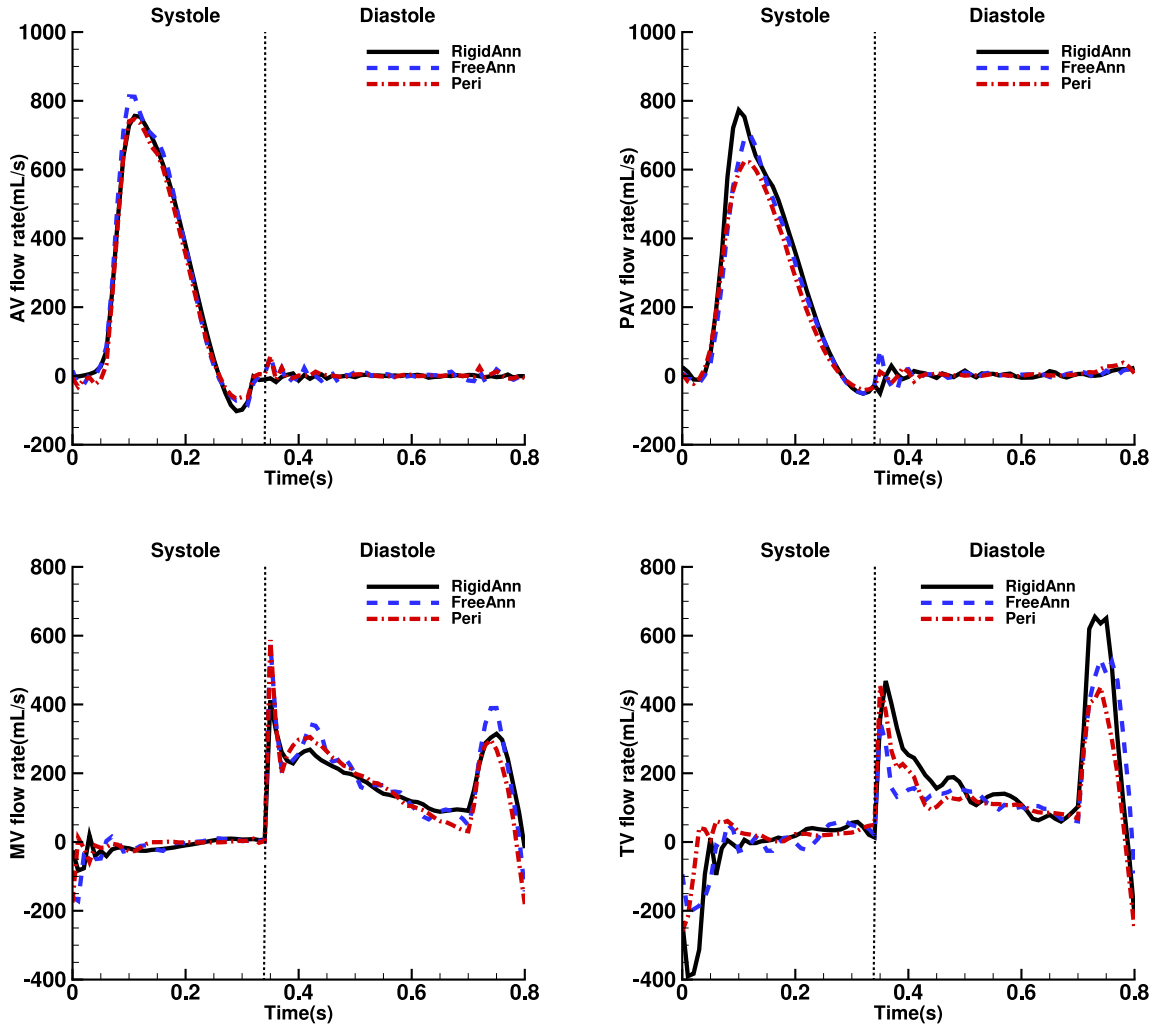

Fig. 24. Transvalvular flow rate at (Top left) AV, (Top right) PAV, (Bottom left) MV and (Bottom right) TV in all cases.

Table 9
Volume increase (dV) in ventricles during early diastolic filling (0.34 s – 0.40 s).

	WH_{Rigid}	WH_{Free}	WH_{Peri}
dV (LV)	17.2 mL	27.2 mL	27.1 mL
dV (RV)	21.7 mL	21.8 mL	26.2 mL

4. Discussions

In this work, we present a four-chamber heart model including physiologically detailed heart valves and fluid–structure interaction analysis. The final model is able to reproduce typical flow patterns within heart chambers which have shown important values in clinical diagnosis and treatment [28,29]. By comparing different modelling assumptions, our results demonstrate the effect of unrestricted valve annular dynamics and pericardium-heart interactions on overall heart performances such as maintaining realistic wall deformation and obtaining better cardiac efficiency in terms of chamber filling and emptying. Most importantly, the current model provides a potential framework for comprehensive multi-physics whole-heart modelling combining all key components such as electrophysiology, tissue mechanics and haemodynamics.

Attempts to develop multi-physics whole-heart models have been made in recent years [18,24,70–72], often focusing on electrophysiology, passive mechanics, active contraction and their interactions. A whole-heart model with fluid–structure interaction is much more challenging because of difficulties in accurately describing valve dynamic performance and their interactions with blood flow. In this regard, some approaches have been developed ranging from lumped parameter models [24] to zero-volumetric immersed surface [33], and to finite-element represented physiologically and anatomically accurate valves [32]. Different from

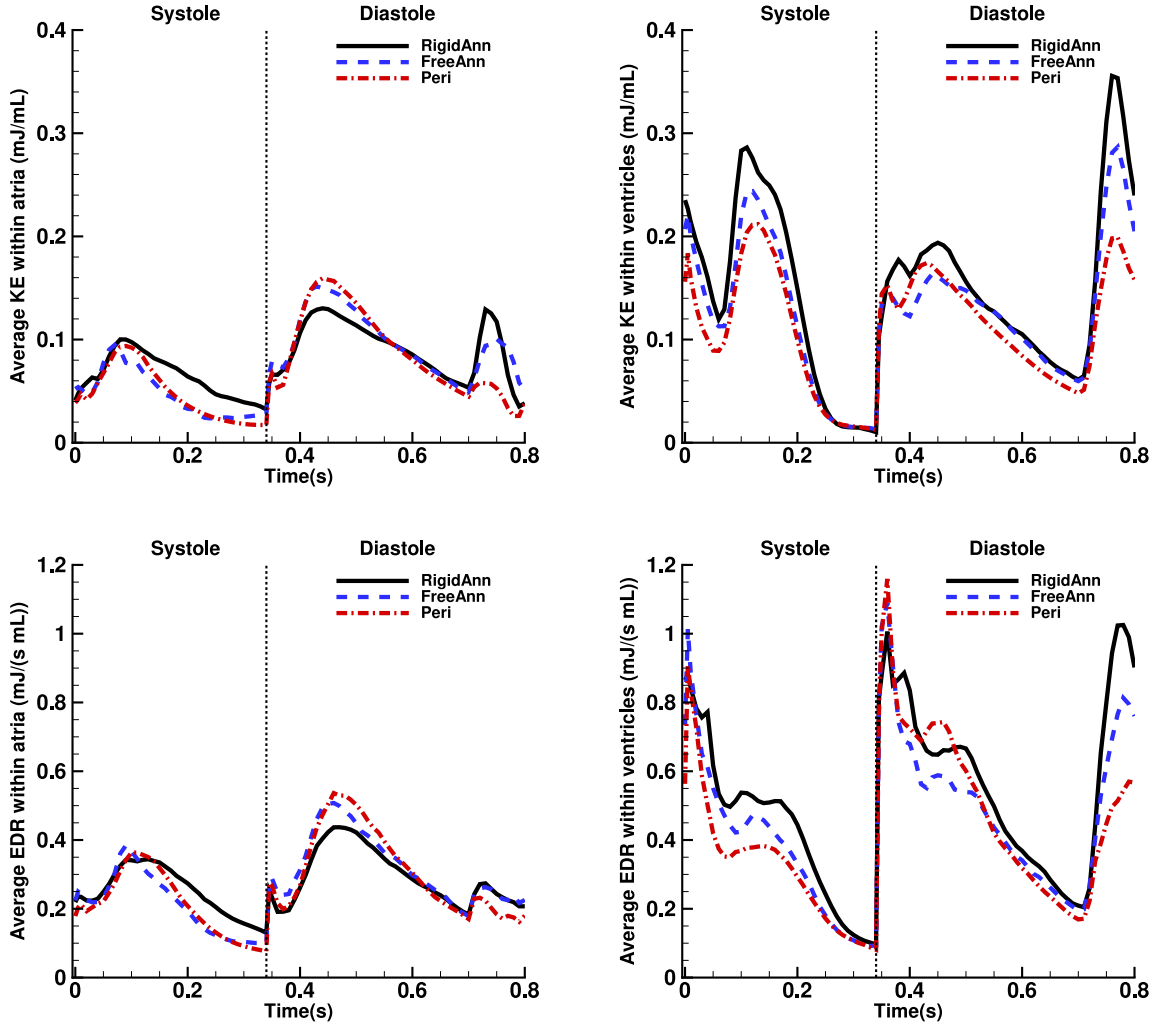

Fig. 25. The average kinetic energy (KE) within (Top left) both atria and (Top right) both ventricles and the average energy dissipation rate (EDR) within (Bottom Left) both atria and (Bottom Right) both ventricles in all cases.

existing studies [68,73,74] where blood flow and valvular dynamics were not considered, we have further investigated the effects of pericardium on cardiac motion and valvular dynamics, this would guide pericardium modelling when developing a personalized whole-heart model.

One major advantage of the current model, compared with other existing whole-heart models, is the incorporation of physiological heart valves together with leaflet-flow interactions captured in the immersed boundary framework. The discussion of valve functions can be divided into two aspects: the role of valve leaflet and valve annulus. In our model, the valve leaflet demonstrates important contributions to ventricular haemodynamics during diastole. For example, the clockwise vortices in LV are formed under clear influences of the MV anterior leaflet which pushes the flow jets towards the LV posterior lateral wall (Fig. 20). Studies have shown that such vorticial flow patterns reduce energy dissipation [75] and blood residence time [75] which can be used as a risk factor for thrombosis. Besides redirecting transvalvular flow, the opening motion of valve leaflets also leads to small vortices formed near leaflet-free edges (Figs. 20 and 21) and such phenomena can only be captured when detailed valve geometry is included. In addition to the effect on flow patterns, a high energy dissipation rate is also found close to the atrial side of MV/TV leaflets during valve opening (Fig. 20). As shown in Fig. 19, the pressure-volume loops during the ventricular isovolumetric phases are not ideal vertical lines. This is attributed to the intricate regulation of valve dynamics within the immersed boundary framework, where fluid–structure interactions govern various factors such as the pressure gradient across the valve and the mechanical properties of valve leaflets. Unlike simplistic lumped-parameter valvular models [70], our approach acknowledges the complexity involved in valve dynamics, making it more challenging to achieve instantaneous opening and closing of valves. This intricate control, crucial in determining the length of isovolumetric periods during ventricular systole, contributes to the observed non-vertical nature of the pressure-volume loops. In fact, the pressure-volume loops in Fig. 19 agree well with clinically measured pressure-volume loops in [76, Figure 2].

In terms of valve annular dynamics, previous studies have shown the annulus shape change throughout the cardiac cycle such as the flattening and expansion during diastole, and shrinking into a saddle shape during systole in the case of MV [77]. Additionally, the left and right atrioventricular plane (LAVP/RAVP) movement along the longitudinal axis is thought to benefit the heart filling and emptying process [78,79]. Our model investigates the importance of annular dynamics by comparing two modelling assumptions: fixed annulus and free annulus. Although two cases lead to similar flow results such as typical LV vortices (Fig. 20), left heart venous flow (Fig. 23) and AV/PAV flow (Fig. 24), our results confirm that allowing annulus expansion and atrioventricular plane movement during early diastole speeds up ventricular filling and atrial emptying as indicated in Fig. 18. In addition, the quantitative measurements shown in Fig. 16 not only reveal the differences between left and right atrioventricular plane movement but also provide a direct and convenient way to compare with clinical image data. Another important finding about annular dynamics is its effect on atrial filling. Although free annulus movement assists heart function during early diastole, our results show that without added pericardial forces, large RAVP longitudinal movement interferes with the RA filling process by creating a compression effect with elevated RA pressure (Fig. 17(Bottom right)) which then leads to reduced inflow from vena cava (Fig. 23).

The influences of pericardium on heart function have been investigated previously but with main focuses on wall deformation [68,73,74]. Its effect on heart haemodynamics is not well elucidated. By incorporating a pericardial boundary traction model, our whole-heart model captures changes in both flow and wall deformation revealing the interactions between heart and surrounding pericardium. Since the chosen spring stiffness (Eq. (19)) for atria is significantly higher than that of ventricles following the approach by Pfaller et al. [68], the predominant effect of added pericardial forces is found on atrial function. For example, our results show that pericardium prevents atrial-free walls from collapsing inwards during atrial contraction (Fig. 14), which leads to enhanced atrioventricular plane movement as a compensation mechanism to assist atrial pumping (Fig. 16(Top row)), and from energy perspective, even though this atrioventricular plane movement contribute to atrial emptying, it does not increase the total kinetic energy stored in blood flow within heart chambers (Fig. 25) which explains why $\mathbf{WH_{Peri}}$ has the smallest late diastolic KE wave among three cases. Similar findings have also been reported in [68,80,81]. Furthermore, the aforementioned mechanism displays an immediate effect on the following atrial filling process: the atrioventricular plane movement towards apex while atrial free walls are being ‘‘pulled’’ by pericardium creates a vacuum effect inside atria which leads to low chamber pressure (Fig. 17(Bottom right)) with earlier and larger systolic inflow from veins (Fig. 23). Finally, by comparing the results between $\mathbf{WH_{Free}}$ and $\mathbf{WH_{Peri}}$, our model suggests that in order to avoid aforementioned atrial chamber compression during systole, it is necessary in the modelling process to consider pericardium-heart interactions while allowing unrestricted annulus movement. In terms of pericardium effect on ventricular function, our results show added pericardial forces lead to reduced systolic peak pressure (Fig. 17(Top row)) and reduced cardiac output (Table 7) suggesting the extra burden on ventricles brought by pericardium during contraction. Another important observation in our results is that the heart walls in both $\mathbf{WH_{Rigid}}$ and $\mathbf{WH_{Free}}$ suffer oscillations especially during rapid filling periods whereas the added pericardial forces in $\mathbf{WH_{Peri}}$ serve as a stabilizer which leads to a steady change in wall deformations throughout cardiac cycle.

Even though direct comparisons with patient-specific data are not available in the current study. Our simulation results show good agreement with literature reports and clinical observations. For example, the peak ventricular systolic pressure in $\mathbf{WH_{Peri}}$ are 102.3 mmHg (LV) and 31.7 mmHg (RV) which fall into the normal range 100–140 mmHg (LV) [82] and 27.8 ± 7.8 mmHg (RV) [83], and the resultant ventricular ejection fractions (48.5% for LV and 46.2% for RV) are close to clinically used normal reference values (52 ± 4% for RV [84] and ≥55% for LV [85]). In terms of valve annular dynamics, our results suggest rapid longitudinal movement at early systole, early diastole and during atrial contraction, which agrees with the clinical measurements by Seemann et al. [86] on Cardiovascular Magnetic Resonance (CMR) images. Additionally, they find that the right atrioventricular plane exhibits larger longitudinal displacement than the left one (2.0 ± 0.4 cm v.s. 1.4 ± 0.3 cm). We observe similar trend in our results in $\mathbf{WH_{Peri}}$ (1.3 cm v.s. 0.7 cm). Also, the biphasic pattern shown in the annulus width plot (Fig. 16) is also confirmed by Maffessanti1 et al. [87] in their study of quantitative evaluation of annular morphology and dynamics. In terms of energy results, Kaur et al. [88] reported similar left ventricular three-wave patterns for KE in a complete cardiac cycle in their systemic review, and by calculating viscous energy loss within left ventricle during diastole using 4DFlow MRI data from healthy volunteers, Elbaz et al. [89] also found similar EDR wave patterns in the left ventricle with an early diastolic wave during rapid filling phase and a late diastolic wave during atrial contraction. It is also worth mentioning that the peak systolic flows for the aortic/pulmonary valve in our model are 747.3 mL/s and 623.6 mL/s, respectively, as shown in Table 8. These values are larger than the reported normal values (427 mL/s for the aortic valve (AV) [90] and 309 mL/s for the pulmonary valve (PAV) [91]), indicating that further improvements are needed in the modelling of ventricular active contraction, valve functionality, and downstream circulation.

The ultimate goal of heart modelling is for clinical translation. One of the biggest obstacles in this process is the cost of numerical simulations. The current model with a solid mesh resolution of 0.125 cm and a fluid mesh resolution of 0.1 cm presents the total degrees of freedom of 18,722,358. The largest time step size is limited to ensure numerical stability throughout the cardiac cycle because of the explicit stepping scheme in our numerical solver [62]. Several factors such as rapid valve opening with large transvalvular flow velocity and large structural deformation could lead to further decreased time step size, which would increase the overall simulation time further. Another important note is that the current study uses surrogate models for active stress generation and does not include a detailed electro-physiology model. To simulate realistic electrical activation with typical monodomain or bidomain models [92], a much finer solid mesh will be required (e.g. 0.02 cm for element edge length) which will significantly increase the overall numerical cost. However, with the fast development of computational techniques, especially artificial intelligent-based surrogate models, i.e. physics-informed neural network [93], the timescale of these numerical simulations could be reduced to be appropriate for clinical applications in the future [94].

4.1. Limitations and perspectives

As mentioned earlier, modelling the whole-heart function is an extremely challenging task and comprises are made in the current model development process for the sake of simplification.

- One limitation in the current study is the pressure boundary conditions applied at vessel boundaries including prescribed venous pressures and Windkessel models at arterial vessels. As a result, the left and right heart in the current model are functioning "independently" in terms of blood circulation. The solution is to incorporate systemic and pulmonary circulation models such as structured tree models [95] into our heart model for a more realistic ventricle-artery pressure gradient and atrium-ventricle pressure gradient [34,96]. This will establish a closed cardiac system with the ability to capture more realistic left–right heart interactions, which possesses great potential in clinical applications. For example, when coupled with pulmonary circulation, our model can provide useful insights into the most common type II pulmonary hypertension [31] (PHLHD). Even though the classic lesion that causes PHLHD is mitral stenosis and regurgitation, the major cause of morbidity and mortality is right heart failure. With detailed haemodynamic information such as pressure and flow, our model can improve understanding of the disease progression which is essential in clinical diagnoses and treatment. Similarly, our whole-heart model can also help with the design of interventional devices such as mechanical/biological valves, and the advantage comes from the ability to capture both local and global haemodynamic effects. As mentioned earlier, the change in valve function affects not only the side of the heart it belongs to but also the other heart chambers.
- Another limitation in the current model is the lack of electrophysiology modelling. The assumed uniform activation in heart chambers can be improved by incorporating detailed electrophysiological models [92,97,98] with ionic activities at the microscale and electrical wave propagation at the macroscale, and also the coupling between electrophysiology and active force generation [18,99].
- Further improvement can be made to the active force generation modelling. For instance, the atrial active contraction model used in this study, despite allowing fine-tuning of both the onset of contraction and the maximum active tension, is not sufficiently realistic. This inadequacy is evident as the atrial pressure-volume (PV) loops in Fig. 19 do not exhibit the characteristic eight-shaped pattern. More sophisticated modelling of atrial contraction is necessary to enhance atrial dynamics, potentially leading to physiologically realistic A-loop and V-loop formations, as discussed in [18]. Additionally, in this work, the active stress models [22,34] neglect the fibres-stretch-rate feedback that may require additional stabilization to avoid numerical instability when included [33]. Such feedback mechanism has been shown to effectively reduce unphysiologically large semilunar valve flow rate [18]. The unrealistic peak systolic flows for both aortic/pulmonary valve obtained in our current model (Fig. 24) are expected to be reduced with the incorporation of this mechanism into our ventricular active contraction modelling.
- Other model limitations such as artificial displacement of chordae origins, lack of valve measurements from original heart geometry and lack of clinical image data for model validations require further attention in future work.

5. Conclusions

We present a computational whole-heart model featuring realistic four-chamber geometry, physiological heart valves, detailed fibre structure, hyperelastic materials and full fluid–structure interaction analysis. Our model is able to simulate physiologically normal heart function by capturing clinically observed haemodynamic behaviours within the heart such as typical left ventricular vortices and less vorticial flow field within the right ventricle, typical venous and transvalvular flow waveform, and physiological heart deformations such as atrioventricular plane movement. The influences of the pericardium on the overall heart function are revealed with a predominant effect on atrial free wall deformation and atrial filling process. Most importantly, the current model provides a framework for electro-mechano-fluidic whole-heart modelling considering all heart valves and fluid–structure interactions.

CRediT authorship contribution statement

Liuyang Feng: Writing – review & editing, Writing – original draft, Visualization, Validation, Software, Resources, Methodology, Investigation, Formal analysis, Data curation, Conceptualization. **Hao Gao:** Writing – review & editing, Supervision, Methodology, Formal analysis. **Xiaoyu Luo:** Writing – review & editing, Supervision, Project administration, Methodology, Funding acquisition, Formal analysis.

Declaration of competing interest

The authors declare that they have no known competing financial interests or personal relationships that could have appeared to influence the work reported in this paper.

Data availability

Data will be made available on request.

Acknowledgements

We gratefully acknowledge the funding provided by the UK EPSRC Established Career Fellowship (EP/S020950/1), the EPSRC International Centre-to-Centre grant (EP/S030875/1), and the British Heart Foundation, United Kingdom (PG/22/10930). We would also like to thank Professor Steven Niederer for the help with the whole-heart geometry dataset.

References

[1] R. Verzicco, Electro-fluid-mechanics of the heart, J. Fluid Mech. 941 (2022).
[2] N.A. Trayanova, Whole-heart modeling: applications to cardiac electrophysiology and electromechanics, Circ. Res. 108 (1) (2011) 113–128.
[3] A. Quarteroni, T. Lassila, S. Rossi, R. Ruiz-Baier, Integrated heart—coupling multiscale and multiphysics models for the simulation of the cardiac function, Comput. Methods Appl. Mech. Engrg. 314 (2017) 345–407.
[4] A. Lopez-Perez, R. Sebastian, J.M. Ferrero, Three-dimensional cardiac computational modelling: Methods, features and applications, Biomed. Eng. Online 14 (1) (2015) 1–31.
[5] S.A. Niederer, J. Lumens, N.A. Trayanova, Computational models in cardiology, Nat. Rev. Cardiol. 16 (2) (2019) 100–111.
[6] A. Suinesiaputra, A.D. McCulloch, M.P. Nash, B. Pontre, A.A. Young, Cardiac image modelling: Breadth and depth in heart disease, Med. Image Anal. 33 (2016) 38–43.
[7] J. Southern, J. Pitt-Francis, J. Whiteley, D. Stokeley, H. Kobashi, R. Nobes, Y. Kadooka, D. Gavaghan, Multi-scale computational modelling in biology and physiology, Progress Biophys. Mol. Biol. 96 (1–3) (2008) 60–89.
[8] H. Gao, H. Wang, C. Berry, X. Luo, B.E. Griffith, Quasi-static image-based immersed boundary-finite element model of left ventricle under diastolic loading, Int. J. Numer. Methods Biomed. Eng. 30 (11) (2014) 1199–1222.
[9] G. Pedrizzetti, F. Domenichini, Left ventricular fluid mechanics: The long way from theoretical models to clinical applications, Ann. Biomed. Eng. 43 (1) (2015) 26–40.
[10] G. Del Corso, R. Verzicco, F. Viola, Sensitivity analysis of an electrophysiology model for the left ventricle, J. R. Soc. Interface 17 (171) (2020) 20200532.
[11] A. Krishnamurthy, C.T. Villongco, J. Chuang, L.R. Frank, V. Nigam, E. Belezzuoli, P. Stark, D.E. Krummen, S. Narayan, J.H. Omens, et al., Patient-specific models of cardiac biomechanics, J. Comput. Phys. 244 (2013) 4–21.
[12] W. Sun, C. Martin, T. Pham, Computational modeling of cardiac valve function and intervention, Ann. Rev. Biomed. Eng. 16 (2014) 53.
[13] H. Gao, N. Qi, L. Feng, X. Ma, M. Danton, C. Berry, X. Luo, Modelling mitral valvular dynamics–current trend and future directions, Int. J. Numer. Methods Biomed. Eng. 33 (10) (2017) e2858.
[14] M. Toma, S. Singh-Gryzbon, E. Frankini, Z. Wei, A.P. Yoganathan, Clinical impact of computational heart valve models, Materials 15 (9) (2022) 3302.
[15] C. Chnafa, S. Mendez, F. Nicoud, Image-based simulations show important flow fluctuations in a normal left ventricle: What could be the implications? Ann. Biomed. Eng. 44 (2016) 3346–3358.
[16] L. Bennati, V. Giambruno, F. Renzi, V. Di Nicola, C. Maffeis, G. Puppini, G.B. Luciani, C. Vergara, Turbulent blood dynamics in the left heart in the presence of mitral regurgitation: A computational study based on multi-series cine-MRI, Biomech. Model. Mechanobiol. (2023) 1–18.
[17] A. Quarteroni, L. Dede', F. Regazzoni, C. Vergara, A mathematical model of the human heart suitable to address clinical problems, Japan J. Ind. Appl. Math. (2023) 1–21.
[18] M. Fedele, R. Piersanti, F. Regazzoni, M. Salvador, P.C. Africa, M. Bucelli, A. Zingaro, A. Quarteroni, et al., A comprehensive and biophysically detailed computational model of the whole human heart electromechanics, Comput. Methods Appl. Mech. Engrg. 410 (2023) 115983.
[19] R. Mittal, J.H. Seo, V. Vedula, Y.J. Choi, H. Liu, H.H. Huang, S. Jain, L. Younes, T. Abraham, R.T. George, Computational modeling of cardiac hemodynamics: Current status and future outlook, J. Comput. Phys. 305 (2016) 1065–1082.
[20] P.C. Franzone, L.F. Pavarino, S. Scacchi, Mathematical Cardiac Electrophysiology. Vol. 13, Springer, 2014.
[21] G.A. Holzapfel, R.W. Ogden, Constitutive modelling of passive myocardium: A structurally based framework for material characterization, Phil. Trans. R. Soc. A 367 (1902) (2009) 3445–3475.
[22] S. Niederer, P. Hunter, N. Smith, A quantitative analysis of cardiac myocyte relaxation: A simulation study, Biophys. J. 90 (5) (2006) 1697–1722.
[23] S.N. Doost, D. Ghista, B. Su, L. Zhong, Y.S. Morsi, Heart blood flow simulation: A perspective review, Biomed. Eng. Online 15 (1) (2016) 1–28.
[24] T. Gerach, S. Schuler, J. Fröhlich, L. Lindner, E. Kovacheva, R. Moss, E.M. Wülfers, G. Seemann, C. Wieners, A. Loewe, Electro-mechanical whole-heart digital twins: A fully coupled multi-physics approach, Mathematics 9 (11) (2021) 1247.
[25] M. Fedele, E. Faggiano, L. Dedè, A. Quarteroni, A patient-specific aortic valve model based on moving resistive immersed implicit surfaces, Biomech. Model. Mechanobiol. 16 (2017) 1779–1803.
[26] H. Gao, L. Feng, N. Qi, C. Berry, B.E. Griffith, X. Luo, A coupled mitral valve—left ventricle model with fluid–structure interaction, Med. Eng. Phys. 47 (2017) 128–136.
[27] D. Collia, L. Zovatto, G. Tonti, G. Pedrizzetti, Comparative analysis of right ventricle fluid dynamics, Front. Bioeng. Biotechnol. 9 (2021) 667408.
[28] S. Hsu, J.C. Fang, B.A. Borlaug, Hemodynamics for the heart failure clinician: A state-of-the-art review, J. Cardiac Failure (2021).
[29] S. Robinson, L. Ring, D.X. Augustine, S. Rekhraj, D. Oxborough, A. Harkness, P. Lancellotti, B. Rana, The assessment of mitral valve disease: A guideline from the British Society of echocardiography, Echo Res. Pract. 8 (1) (2021) G87–G136.
[30] C. Mihl, W. Dassen, H. Kuipers, Cardiac remodelling: Concentric versus eccentric hypertrophy in strength and endurance athletes, Netherlands Heart J. 16 (2008) 129–133.
[31] N. Galiè, M. Humbert, J.-L. Vachiery, S. Gibbs, I. Lang, A. Torbicki, G. Simonneau, A. Peacock, A. Vonk Noordegraaf, M. Beghetti, et al., 2015 ESC/ERS guidelines for the diagnosis and treatment of pulmonary hypertension: The joint task force for the diagnosis and treatment of pulmonary hypertension of the European Society of Cardiology (ESC) and the European respiratory society (ERS): Endorsed by: Association for European paediatric and congenital cardiology (AEPC), International Society for Heart and Lung Transplantation (ISHLT), Eur. Heart J. 37 (1) (2016) 67–119.
[32] M. Davey, C. Puelz, S. Rossi, M.A. Smith, D.R. Wells, G. Sturgeon, W.P. Segars, J.P. Vavalle, C.S. Peskin, B.E. Griffith, Simulating cardiac fluid dynamics in the human heart, 2023, arXiv preprint arXiv:2307.02680.
[33] A. Zingaro, M. Bucelli, R. Piersanti, F. Regazzoni, L. Dede, A. Quarteroni, An electromechanics-driven fluid dynamics model for the simulation of the whole human heart, 2023, arXiv preprint arXiv:2301.02148.
[34] L. Feng, H. Gao, N. Qi, M. Danton, N.A. Hill, X. Luo, Fluid–structure interaction in a fully coupled three-dimensional mitral–atrium–pulmonary model, Biomech. Model. Mechanobiol. 20 (4) (2021) 1267–1295.
[35] M. Strocchi, C.M. Augustin, M.A. Gsell, E. Karabelas, A. Neic, K. Gillette, O. Razeghi, A.J. Prassl, E.J. Vigmond, J.M. Behar, et al., A publicly available virtual cohort of four-chamber heart meshes for cardiac electro-mechanics simulations, PLoS One 15 (6) (2020) e0235145.
[36] J. Landsberg, Manual for Pulmonary and Critical Care Medicine E-Book, Elsevier Health Sciences, 2017.
[37] F. Haddad, S.A. Hunt, D.N. Rosenthal, D.J. Murphy, Right ventricular function in cardiovascular disease, part I: Anatomy, physiology, aging, and functional assessment of the right ventricle, Circulation 117 (11) (2008) 1436–1448.

[38] M. Hadjicharalambous, C.T. Stoeck, M. Weisskopf, N. Cesarovic, E. Ioannou, V. Vavourakis, D.A. Nordsletten, Investigating the reference domain influence in personalised models of cardiac mechanics: Effect of unloaded geometry on cardiac biomechanics, Biomech. Model. Mechanobiol. 20 (4) (2021) 1579–1597.
[39] H. Wang, X. Luo, H. Gao, R. Ogden, B. Griffith, C. Berry, T. Wang, A modified Holzapfel-Ogden law for a residually stressed finite strain model of the human left ventricle in diastole, Biomech. Model. Mechanobiol. 13 (1) (2014) 99–113.
[40] L. Feng, N. Qi, H. Gao, W. Sun, M. Vazquez, B.E. Griffith, X. Luo, On the chordae structure and dynamic behaviour of the mitral valve, IMA J. Appl. Math. 83 (6) (2018) 1066–1091.
[41] Q. Wang, W. Sun, Finite element modeling of mitral valve dynamic deformation using patient-specific multi-slices computed tomography scans, Ann. Biomed. Eng. 41 (1) (2013) 142–153.
[42] M. Stevanella, E. Votta, M. Lemma, C. Antona, A. Redaelli, Finite element modelling of the tricuspid valve: A preliminary study, Med. Eng. Phys. 32 (10) (2010) 1213–1223.
[43] M.E. Hiro, J. Jouan, M.R. Pagel, E. Lansac, K.H. Lim, H.-S. Lim, C.M. Duran, Sonometric study of the normal tricuspid valve annulus in sheep, J. Heart Valve Dis. 13 (3) (2004) 452–460.
[44] H. Reul, A. Vahlbruch, M. Giersiepen, T. Schmitz-Rode, V. Hirtz, S. Effert, The geometry of the aortic root in health, at valve disease and after valve replacement, J. Biomech. 23 (2) (1990) 181–191.
[45] C.S. Peskin, D.M. McQUEEN, Mechanical equilibrium determines the fractal fiber architecture of aortic heart valve leaflets, Am. J. Physiol.-Heart Circ. Physiol. 266 (1) (1994) H319–H328.
[46] B.E. Griffith, Immersed boundary model of aortic heart valve dynamics with physiological driving and loading conditions, Int. J. Numer. Methods Biomed. Eng. 28 (3) (2012) 317–345.
[47] P. Stradins, R. Lacis, I. Ozolanta, B. Purina, V. Ose, L. Feldmane, V. Kasyanov, Comparison of biomechanical and structural properties between human aortic and pulmonary valve, Eur. J. Cardio-Thoracic Surg. 26 (3) (2004) 634–639.
[48] S.Y. Ho, R.H. Anderson, D. Sánchez-Quintana, Atrial structure and fibres: Morphologic bases of atrial conduction, Cardiovasc. Res. 54 (2) (2002) 325–336.
[49] R. Greenbaum, S.Y. Ho, D. Gibson, A. Becker, R. Anderson, Left ventricular fibre architecture in man, Heart 45 (3) (1981) 248–263.
[50] S. Ho, P. Nihoyannopoulos, Anatomy, echocardiography, and normal right ventricular dimensions, Heart 92 (suppl 1) (2006) i2–i13.
[51] D. Rohmer, A. Sitek, G.T. Gullberg, Reconstruction and visualization of fiber and laminar structure in the normal human heart from ex vivo diffusion tensor magnetic resonance imaging (DTMRI) data, Invest. Radiol. 42 (11) (2007) 777–789.
[52] J.D. Bayer, R.C. Blake, G. Plank, N.A. Trayanova, A novel rule-based algorithm for assigning myocardial fiber orientation to computational heart models, Ann. Biomed. Eng. 40 (10) (2012) 2243–2254.
[53] M.W. Krueger, V. Schmidt, C. Tobón, F.M. Weber, C. Lorenz, D.U. Keller, H. Barschdorf, M. Burdumy, P. Neher, G. Plank, et al., Modeling atrial fiber orientation in patient-specific geometries: A semi-automatic rule-based approach, in: International Conference on Functional Imaging and Modeling of the Heart, Springer, 2011, pp. 223–232.
[54] R. Piersanti, P.C. Africa, M. Fedele, C. Vergara, L. Dedè, A.F. Corno, A. Quarteroni, Modeling cardiac muscle fibers in ventricular and atrial electrophysiology simulations, Comput. Methods Appl. Mech. Engrg. 373 (2021) 113468.
[55] D. Scollan, A. Holmes, J. Zhang, R. Winslow, Reconstruction of cardiac ventricular geometry and fiber orientation using magnetic resonance imaging, Ann. Biomed. Eng. 28 (2000) 934–944.
[56] I.J. LeGrice, Y. Takayama, J. Covell, Transverse shear along myocardial cleavage planes provides a mechanism for normal systolic wall thickening, Circ. Res. 77 (1) (1995) 182–193.
[57] J.M. Hoermann, M.R. Pfaller, L. Avena, C. Bertoglio, W.A. Wall, Automatic mapping of atrial fiber orientations for patient-specific modeling of cardiac electromechanics using image registration, Int. J. Numer. Methods Biomed. Eng. 35 (6) (2019) e3190.
[58] C.H. Roney, R. Bendikas, F. Pashakhanloo, C. Corrado, E.J. Vigmond, E.R. McVeigh, N.A. Trayanova, S.A. Niederer, Constructing a human atrial fibre atlas, Ann. Biomed. Eng. 49 (2021) 233–250.
[59] L. Feng, H. Gao, B. Griffith, S. Niederer, X. Luo, Analysis of a coupled fluid-structure interaction model of the left atrium and mitral valve, Int. J. Numer. Methods Biomed. Eng. 35 (11) (2019) e3254.
[60] L.T. Hudson, S.V. Jett, K.E. Kramer, D.W. Laurence, C.J. Ross, R.A. Towner, R. Baumwart, K.M. Lim, A. Mir, H.M. Burkhart, et al., A pilot study on linking tissue mechanics with load-dependent collagen microstructures in porcine tricuspid valve leaflets, Bioengineering 7 (2) (2020) 60.
[61] C.S. Peskin, The immersed boundary method, Acta Numer. 11 (2002) 479–517.
[62] B.E. Griffith, X. Luo, Hybrid finite difference/finite element immersed boundary method, Int. J. Numer. Methods Biomed. Eng. 33 (12) (2017) e2888.
[63] B. Vadala-Roth, S. Acharya, N.A. Patankar, S. Rossi, B.E. Griffith, Stabilization approaches for the hyperelastic immersed boundary method for problems of large-deformation incompressible elasticity, Comput. Methods Appl. Mech. Engrg. 365 (2020) 112978.
[64] A. Borowska, H. Gao, A. Lazarus, D. Husmeier, Bayesian optimisation for efficient parameter inference in a cardiac mechanics model of the left ventricle, Int. J. Numer. Methods Biomed. Eng. (2022) e3593.
[65] R.H. Keldermann, M.P. Nash, H. Gelderblom, V.Y. Wang, A.V. Panfilov, Electromechanical wavebreak in a model of the human left ventricle, Am. J. Physiol.-Heart Circ. Physiol. 299 (1) (2010) H134–H143.
[66] T.C. Gasser, R.W. Ogden, G.A. Holzapfel, Hyperelastic modelling of arterial layers with distributed collagen fibre orientations, J. R. Soc. Interface 3 (6) (2006) 15–35.
[67] T. Koch, B. Reddy, P. Zilla, T. Franz, Aortic valve leaflet mechanical properties facilitate diastolic valve function, Comput, Methods Biomech. Biomed. Eng. 13 (2) (2010) 225–234.
[68] M.R. Pfaller, J.M. Hörmann, M. Weigl, A. Nagler, R. Chabiniok, C. Bertoglio, W.A. Wall, The importance of the pericardium for cardiac biomechanics: From physiology to computational modeling, Biomech. Model. Mechanobiol. 18 (2) (2019) 503–529.
[69] P. Segers, E. Rietzschel, M. De Buyzere, N. Stergiopulos, N. Westerhof, L. Van Bortel, T. Gillebert, P. Verdonck, Three-and four-element windkessel models: Assessment of their fitting performance in a large cohort of healthy middle-aged individuals, Proc. Inst. Mech. Eng., Part H: J. Eng. Med. 222 (4) (2008) 417–428.
[70] B. Baillargeon, N. Rebelo, D.D. Fox, R.L. Taylor, E. Kuhl, The living heart project: A robust and integrative simulator for human heart function, Eur. J. Mech. A Solids 48 (2014) 38–47.
[71] C.M. Augustin, A. Neic, M. Liebmann, A.J. Prassl, S.A. Niederer, G. Haase, G. Plank, Anatomically accurate high resolution modeling of human whole heart electromechanics: A strongly scalable algebraic multigrid solver method for nonlinear deformation, J. Comput. Phys. 305 (2016) 622–646.
[72] S. Land, S.A. Niederer, Influence of atrial contraction dynamics on cardiac function, Int. J. Numer. Methods Biomed. Eng. 34 (3) (2018) e2931.
[73] T. Fritz, C. Wieners, G. Seemann, H. Steen, O. Dössel, Simulation of the contraction of the ventricles in a human heart model including atria and pericardium, Biomech. Model. Mechanobiol. 13 (3) (2014) 627–641.
[74] M. Strocchi, M.A. Gsell, C.M. Augustin, O. Razeghi, C.H. Roney, A.J. Prassl, E.J. Vigmond, J.M. Behar, J.S. Gould, C.A. Rinaldi, et al., Simulating ventricular systolic motion in a four-chamber heart model with spatially varying robin boundary conditions to model the effect of the pericardium, J. Biomech. 101 (2020) 109645.
[75] S. Hendabadi, J. Bermejo, Y. Benito, R. Yotti, F. Fernández-Avilés, J.C. Del Álamo, S.C. Shadden, Topology of blood transport in the human left ventricle by novel processing of Doppler echocardiography, Ann. Biomed. Eng. 41 (2013) 2603–2616.

[76] T. Patterson, S. Rivolo, D. Burkhoff, J. Schreuder, N. Briceno, C. Allen, R. Williams, S. Arri, K.N. Asrress, J. Joseph, et al., Physiological impact of afterload reduction on cardiac mechanics and coronary hemodynamics following isosorbide dinitrate administration in ischemic heart disease, J. Cardiovasc. Transl. Res. (2021) 1–13.
[77] S.E. van Wijngaarden, V. Kamperidis, M.V. Regeer, M. Palmen, M.J. Schalij, R.J. Klautz, J.J. Bax, N. Ajmone Marsan, V. Delgado, Three-dimensional assessment of mitral valve annulus dynamics and impact on quantification of mitral regurgitation, Eur. Heart J.-Cardiovasc. Imaging 19 (2) (2018) 176–184.
[78] M. Carlsson, M. Ugander, H. Mosén, T. Buhre, H. Arheden, Atrioventricular plane displacement is the major contributor to left ventricular pumping in healthy adults, athletes, and patients with dilated cardiomyopathy, Am. J. Physiol.-Heart Circ. Physiol. 292 (3) (2007) H1452–H1459.
[79] E. Maksuti, A. Bjällmark, M. Broomé, Modelling the heart with the atrioventricular plane as a piston unit, Med. Eng. Phys. 37 (1) (2015) 87–92.
[80] M. Carlsson, E. Heiberg, J. Toger, H. Arheden, Quantification of left and right ventricular kinetic energy using four-dimensional intracardiac magnetic resonance imaging flow measurements, Am. J. Physiol.-Heart Circ. Physiol. 302 (4) (2012) H893–H900.
[81] P.M. Arvidsson, J. Töger, E. Heiberg, M. Carlsson, H. Arheden, Quantification of left and right atrial kinetic energy using four-dimensional intracardiac magnetic resonance imaging flow measurements, J. Appl. Physiol. 114 (10) (2013) 1472–1481.
[82] M.E. Klingensmith, et al., The Washington Manual of Surgery, Lippincott Williams & Wilkins, 2008.
[83] D.W. Armstrong, M.F. Matangi, Estimated right ventricular systolic pressure during exercise stress echocardiography in patients with suspected coronary artery disease, Canad. J. Cardiol. 26 (2) (2010) e45–e49.
[84] S. Chua, R.A. Levine, C. Yosefy, M.D. Handschumacher, J. Chu, A. Qureshi, J. Neary, T.-T. Ton-Nu, M. Fu, C.J. Wu, et al., Assessment of right ventricular function by real-time three-dimensional echocardiography improves accuracy and decreases interobserver variability compared with conventional two-dimensional views, Eur. J. Echocardiogr. 10 (5) (2009) 619–624.
[85] C.S. Lam, S.D. Solomon, Classification of heart failure according to ejection fraction: Jacc review topic of the week, J. Am. Coll. Cardiol. 77 (25) (2021) 3217–3225.
[86] F. Seemann, U. Pahlm, K. Steding-Ehrenborg, E. Ostenfeld, D. Erlinge, J.-L. Dubois-Rande, S.E. Jensen, D. Atar, H. Arheden, M. Carlsson, et al., Time-resolved tracking of the atrioventricular plane displacement in cardiovascular magnetic resonance (CMR) images, BMC Med. Imaging 17 (2017) 1–16.
[87] F. Maffessanti, P. Gripari, G. Pontone, D. Andreini, E. Bertella, S. Mushtaq, G. Tamborini, L. Fusini, M. Pepi, E.G. Caiani, Three-dimensional dynamic assessment of tricuspid and mitral annuli using cardiovascular magnetic resonance, Eur. Heart J.–Cardiovasc. Imaging 14 (10) (2013) 986–995.
[88] H. Kaur, H. Assadi, S. Alabed, D. Cameron, V.S. Vassiliou, J.J. Westenberg, R. van der Geest, L. Zhong, A. Dastidar, A.J. Swift, et al., Left ventricular blood flow kinetic energy assessment by 4D flow cardiovascular magnetic resonance: A systematic review of the clinical relevance, J. Cardiovasc. Dev. Dis. 7 (3) (2020) 37.
[89] M.S. Elbaz, R.J. van der Geest, E.E. Calkoen, A. de Roos, B.P. Lelieveldt, A.A. Roest, J.J. Westenberg, Assessment of viscous energy loss and the association with three-dimensional vortex ring formation in left ventricular inflow: In vivo evaluation using four-dimensional flow MRI, Magn. Resonance Med. 77 (2) (2017) 794–805.
[90] K. Hammermeister, R. Brooks, J. Warbasse, The rate of change of left ventricular volume in man: I. Validation and peak systolic ejection rate in health and disease, Circulation 49 (4) (1974) 729–738.
[91] N. Abolmaali, A. Esmaeili, P. Feist, H. Ackermann, M. Requardt, H. Schmidt, T. Vogl, Reference values of MRI flow measurements of the pulmonary outflow tract in healthy children, RoFo: Fortschritte auf dem Gebiete der Rontgenstrahlen und der Nuklearmedizin 176 (6) (2004) 837–845.
[92] M. Potse, B. Dubé, J. Richer, A. Vinet, R.M. Gulrajani, A comparison of monodomain and bidomain reaction-diffusion models for action potential propagation in the human heart, IEEE Trans. Biomed. Eng. 53 (12) (2006) 2425–2435.
[93] D. Dalton, D. Husmeier, H. Gao, Physics-informed graph neural network emulation of soft-tissue mechanics, Comput. Methods Appl. Mech. Engrg. 417 (2023) 116351.
[94] J. Corral-Acero, F. Margara, M. Marciniak, C. Rodero, F. Loncaric, Y. Feng, A. Gilbert, J.F. Fernandes, H.A. Bukhari, A. Wajdan, et al., The 'digital twin'to enable the vision of precision cardiology, Eur. heart J. 41 (48) (2020) 4556–4564.
[95] M.U. Qureshi, G.D. Vaughan, C. Sainsbury, M. Johnson, C.S. Peskin, M.S. Olufsen, N. Hill, Numerical simulation of blood flow and pressure drop in the pulmonary arterial and venous circulation, Biomech. Model. Mechanobiol. 13 (5) (2014) 1137–1154.
[96] W. Chen, H. Gao, X. Luo, N. Hill, Study of cardiovascular function using a coupled left ventricle and systemic circulation model, J. Biomech. 49 (12) (2016) 2445–2454.
[97] A. Bueno-Orovio, E.M. Cherry, F.H. Fenton, Minimal model for human ventricular action potentials in tissue, J. Theoret. Biol. 253 (3) (2008) 544–560.
[98] P. Colli Franzone, L. Pavarino, G. Savaré, Computational electrocardiology: Mathematical and numerical modeling, Complex Syst. Biomed. (2006) 187–241.
[99] F. Regazzoni, A. Quarteroni, An oscillation-free fully partitioned scheme for the numerical modeling of cardiac active mechanics, 2020, arXiv preprint arXiv:2007.15714.